



# EFECTOS SISTEMÁTICOS EN FUTUROS EXPERIMENTOS DE POLARIZACIÓN DEL CMB PARA LA DETECCIÓN DE LAS ONDAS GRAVITACIONALES PRIMORDIALES

## (Systematic effects in the future CMB polarization experiments for the detection of the primordial gravitational waves)

**Trabajo de Fin de Máster**
**para acceder al**

**MÁSTER EN FÍSICA DE PARTÍCULAS Y DEL COSMOS**

**Autor: Jun-Yan ZHANG**

**Director: Enrique MARTÍNEZ GONZÁLEZ**

**julio - 2021**

UNIVERSIDAD DE CANTABRIA
&
UNIVERSIDAD INTERNACIONAL MENÉNDEZ PELAYO

MASTER THESIS

# Systematic effects in future CMB polarization experiments for the detection of the primordial gravitational waves
# -
# Efectos sistemáticos en futuros experimentos de polarización del CMB para la detección de las ondas gravitacionales primordiales

*Author:*
Jun-Yan ZHANG

*Supervisor:*
Prof. Enrique MARTÍNEZ-GONZÁLEZ

Observational Cosmology and Instrumentation Group
Instituto de Física de Cantabria

July 23, 2021

**Systematic effects in future CMB polarization experiments for the detection of the primordial gravitational waves**

**-**

**Efectos sistemáticos en futuros experimentos de polarización del CMB para la detección de las ondas gravitacionales primordiales**

by Jun-Yan ZHANG

# *Abstract*

The B-mode pattern of the polarization of the Cosmic Microwave Background (CMB) is the imprint of the Primordial Gravitational Waves (PGW) during the inflation period. Nowadays, several experiments have been dedicated to observe the B-mode polarization signal but it has not been discovered yet. In the future, there will be some new experiments specialized in detecting the CMB polarization, touching the 0.001 limit of the parameter $r$, the tensor-to-scalar ratio which is an indicator about the strength of PGW. The weak signal from B-mode polarization together with the noises and systematic effects make the detection extremely hard. In this paper, we mainly evaluated the different influences of three relevant systematic effects, polarization angle mismatch, pointing error and beam calibration imperfection acting on four future experiments: LiteBIRD, PICO, Simons Observatory and CMB Stage-4. We showed that to reach an 1% increment in the uncertainty (error) in the parameter $r$, the polarization angle should be calibrated within 3′-22′ and the pointing direction should be calibrated within 1′-4′, depending on the experiment. On the other hand, the uncertainties in the beam calibration of the sidelobes affect the error in $r$ in a wide range from 0.05% to 200% for the different experiments.

**Keywords:** Cosmic Microwave Background, Polarization, B-mode, Instrumentation, Systematic effects

El patrón de polarización del Fondo Cósmico de Microondas (CMB) dado por el modo B representa la huella dejada por las Ondas Gravitacionales Primigenias (PGW) durante el periodo inflacionario. Actualmente, varios experimentos han sido dedicados a observar la señal del modo B de polarización pero no ha sido descubierta todavía. En el futuro, habrá nuevos experimentos especializados en detectar la polarización del CMB, alcanzando el límite de 0.001 en el parámetro $r$, la razón tensorial-scalar que es un indicador de la amplitud de las PGW. La débil señal del modo B de polarización junto con el ruido instrumental y los efectos sistemáticos hacen que la detección sea extremadamente difícil. En este trabajo, consideramos la influencia de tres efectos sistemáticos relevantes, el desajuste en el ángulo de polarización, el error del apuntado y la incertidumbre en la calibración del haz, actuando sobre cuatro experimentos futuros: LiteBIRD, PICO, Simons Observatory y CMB Stage-4. Se muestra que para alcanzar un incremento del 1% en la incertidumbre del parámetro $r$, el ángulo de polarización debería de ser calibrado en el rango $3' - 22'$ y la dirección en el apuntado debería de ser calibrada en el rango $1' - 4'$, dependiendo del experimento. Por otro lado, las incertidumbres en la calibración de los lóbulos laterales del haz afectan al error en $r$ en un rango amplio desde 0.05% hasta 200% para los diferentes experimentos.

**Palabras clave:** . El Fondo Cósmico de Microondas, Polarización, modos B, Instrumentación, Efectos sistemáticos

# *Acknowledgements*

I am here by to thank my dear supervisor Prof. Enrique MARTÍNEZ-GONZÁLEZto spend infinite time teaching me and discussing the physics with me. Thanks to the kind help from Prof. Patricio VIELVA, Prof. Belén BARREIRO, Patricia DIEGO in the Observational Cosmology and Instrumentation Group. With the foundation and scholarship provided by CSIC JAE intro 2020, this research project could become possible. I also would like to appreciate the encouragement from my classmates and partners, Yimi Perla, Roberto Guerrero and Rufa Rafeek in the same master projects.

# Contents

# List of Figures

# List of Tables

# List of Abbreviations

| | |
|---|---|
| **CMB** | **C**osmic **M**icrowave **B**ackground |
| **LSS** | **L**ast **S**cattering **S**urface |
| **GW** | **G**ravitational **W**ave |
| **PGWB** | **P**rimordial **G**ravitational **W**ave **B**-mode |
| **GW** | **G**ravitational **W**ave |
| **FSL** | **F**ar-**S**ide**L**obe |
| **FWHM** | **F**ull **W**idth **H**alf **M**aximum |
| **COBE** | **CO**smic **B**ackground **E**xplorer |
| **WMAP** | **W**ilkinson **M**icrowave **A**nisotropy **P**robe |
| **LiteBIRD** | **Lite** (Light) satellite for the studies of **B**-mode polarization and **I**nfation from cosmic background **R**adiation **D**etection |
| **CMB-S4** | **CMB S**tage-**4** |
| **DW** | **D**eep and **W**ide (measurement) |
| **UD** | **U**ltra-**D**eep (measurement) |
| **SO** | **S**imons **O**bservatory |
| **SAT** | **S**mall **A**perture **T**elescope |
| **LAT** | **L**arge **A**perture **T**elescope |
| **PICO** | The **P**robe of **I**nflation and **C**osmic **O**rigins |
| **HPC** | **H**igh **P**erformance and **C**omputing |
| **LISA** | **L**aser **I**nterferometer **S**pace **A**ntenna |
| **LIGO** | **L**aser **I**nterferometer **G**ravitational-Wave **O**bservatory |

# Chapter 1

# Introduction to the CMB polarization

## 1.1 Background

In 1965, Penzias A.A. and Wilson R.W. made a milestone discovery in the cosmological research history using the Homdel Horn Antenna (a microwave telescope) and in turn they were awarded with 1978 Nobel Prize in Physics. They found there is an isotropic, unpolarized radiation with a temperature around 3K and free from the seasonal variation[1].

The Princeton group, including the 2019 Nobel Laureate James Peebles, interpreted this isotropic radiation as the CMB, the radiation predicted in the Big Bang model. The sensitivity of the antenna at 60s was too low and the noise was too high to detect any anisotropic detail of the CMB. However, despite the dipole anisotropy caused by the peculiar velocity of our planet respect to the Last Scattering Surface (LSS) first predicted in 1969[2], the intrinsic deviations from isotropy expected in the Big Bang model to explain the observed inhomogeneities in the universe were not discovered until 1992. In this year, George F. Smoot lead the team of the Differential Microwave Radiometer experiment onboard the Cosmic Background Explorer (COBE), found the weak anisotropic signal of the CMB in a scale around 7 degrees[3] and then he was awarded with the 2006 Nobel Prize. In the following years, more detailed anisotropies of CMB were discovered with instruments like Wilkinson Microwave Anisotropy Probe (WMAP) and Planck satellite etc. The anisotropies are related to the perturbations at the early universe, according to the inflation theory, a theory which is somewhat speculative (lacking a solid physical foundation and observational evidence) but useful to explain several fundamental properties of the present universe that remained otherwise inexplicable within the Big Bang model.

Besides, the polarization signal which was omitted also due to poor instrumental sensitivity in the first glimpse to the CMB, was discovered with its anisotropies in 2002 by J.M.Kovac et al. using the Degree Angular Scale Interferometer (DASI) at the South Pole[4] and then was followed up by WMAP and Planck with much better precision and resolutions. The CMB is about 10% polarized.

All of the modern models describing our universe should take the CMB into account and have a reasonable, convincing explanation for that.

Raised by Alan H. Guth in 1980, inflation model describes that the inflation is an scenario in which the universe is in an accelerating expansion that happened at a short time after the Big Bang and driven by a field called inflaton[5]. It is such a successful theory that can elegantly solve three main cosmological problems: (1) the horizon problem, i.e., the early universe is assumed to be highly homogeneous, in spite of the fact that separated regions were causally disconnected; (2) the flatness problem, i.e., the initial value of the curvature must be fine tuned to extraordinary

accuracy to produce a universe as flat as the one we see today[5] and (3) magnetic monopole problem, i.e., the existence of magnetic monopoles is predicted by many theories but there is no experimental or observational sign of them[6]. However, inflation has not been sufficiently certified or proved by observations yet. Scientists believe that the CMB anisotropy is induced by the perturbation at the early universe and then stretched out by inflation, forming the seeds for the structure formation at a later time. The stretched perturbation left some imprint at the last scattering surface, where the photons firstly became free to travel and Thomson scattering between photons and electrons provided some polarization signal due to anisotropy of the incoming light.

CMB polarization can be categorized into two patterns: E-mode (behaves like a gradient) and B-mode (behaves like a curl). E-mode was produced by both scalar perturbation (density waves fluctuations) and tensor perturbations (primordial gravitational waves or PGW) at the early universe. B-modes, on the other hand, was only generated by tensor perturbations. The amplitude ratio between the two modes is described by the tensor-to-scalar ratio $r$. The parameter $r$ and spectral indices from scalar perturbations and tensor perturbations, $n_s$ and $n_t$ are crucial to determine the parameters of the inflaton potential $v$. Nowadays, the constraint on the tensor-to-scalar ratio $r$ is set to be $< 0.044$ by the unprecedently precise instrument Planck satellite and BICEP/Keck array[7].

## 1.2 The Origin of CMB Black-Body Radiation

Although we mentioned about the CMB anisotropies, the amplitude of the anisotropies is around 300 micro-Kelvin, relative to the 2.7 Kelvin, the fluctuation $\Theta = \frac{\Delta T}{T}$ is at a level of $10^{-5}$. Thus at first sight we saw a nearly perfect black-body radiation, as Penzias observed in 1965.

The story of the CMB begins at the Last Scattering Surface (LSS). During the expansion, the photon traveling through the entire universe will suffer from the cosmological red-shift; as the following formula indicates, the energy $E$ change inversely proportional to the scale factor as a function of the red-shift $a(z)$[8]: $E \propto \frac{1}{a(z)}$.

However, before the LSS the very early universe was opaque: the universe was so hot that the photons were continuously scattered with electrons forming a hot plasma soup, and the photons did not have a long enough free path to travel.

According to the continuity equation and the equation of state of matter and radiation, the energy density of ordinary matter and photons will decrease while the universe expands (increasing scale factor)[8][9], and so does the temperature of the universe.

Once the universe was cooled down enough, protons, neutrons and electrons first become bound forming atoms allowing photons to travel freely. This period is called recombination and happens in a sudden relative to a cosmological time scale[10].

The CMB is the red-shifted light from this time, and observed by us from the present time; it comes from all directions of the sky just as if there were a very distant radiating surface, the LSS. The temperature at that time is determined by the Saha ionization equation, which describes the thermodynamics of a chemical equilibrium system and was derived in 1921[11]. For more details on the conditions to apply that equation to the early universe see [10]. The temperature at the recombination is determined to be 3000 Kelvin, arround 1/4 eV. Then the corresponding redshift value of the LSS can be also established to be $z = 1100$ by comparing to the 2.7

Kelvin CMB temperature observational result. This information allows us to know that Recombination happens arround 380000 years after the Big Bang. According to the Planck law, the CMB observational black-body temperature is[9]:

$$T_b = \frac{h\nu}{k} \ln^{-1}\left(1 + \frac{2h\nu^3}{I_\nu c^2}\right). \tag{1.1}$$

Its near isotropy is a natural result from the Friedmann-Lemaître-Robertson-Walker (FLRW) metric, and can be considered as a justification of the cosmological principle: that the spatial distribution of matter in the universe is homogeneous and isotropic when viewed on a large enough scale[12] (although there were some dissenting voices[13]).

## 1.3 The Polarization

CMB is expected to be around 10% linearly polarized due to Thompson scattering of photons off free electrons in the LSS. Below we will explain the basic processes that took place in the generation of the CMB polarization and provide some basic concepts and parameters related to the formalism commonly used for its analysis.

### 1.3.1 Thomson scattering

Thomson scattering is the process by which an electron emits dipole radiation due to the oscillation induced by the incoming electromagnetic field, which can be regarded as a low-energy approximation of the Compton scattering.

Thomson scattering is linearly polarized along the electron oscillation direction, and the intensity of the outgoing beam, forming an angle $\beta$ with the incident beam, is proportional to $\cos^2\beta$ if the polarization vector lies in the scattering plane. If the incident light is isotropic there will not be any preference polarization direction of the outgoing light. However, the radiation anisotropy was introduced due to the presence of perturbations at the beginning of the universe, and today we detected there is some net polarization in CMB. We are going to explore the polarization in a mathematical way below.

### 1.3.2 Stokes parameters

The state of polarization of electromagnetic radiation is usually described in terms of the Stokes parameters, which were introduced by G.G. Stokes in 1825[14].

Following[15], a right-handed orthogonal system $\left(\boldsymbol{\epsilon}^{(1)}, \boldsymbol{\epsilon}^{(2)}, \boldsymbol{n}\right)$ can be used to describe the propagation of an electromagnetic wave with the electric field $\boldsymbol{E} = E_1\boldsymbol{\epsilon}^{(1)} + E_2\boldsymbol{\epsilon}^{(2)}$ in the direction of $\boldsymbol{n}$ and with defined polarization directions $\boldsymbol{\epsilon}^{(1)}$ and $\boldsymbol{\epsilon}^{(2)}$.

The polarization tensor is defined as

$$P_{ij} = E_a^* E_b \boldsymbol{\epsilon}_i^{(1)} \boldsymbol{\epsilon}_j^{(1)}, \tag{1.2}$$

and from this equation we can extract out a Hermitian $2 \times 2$ matrix and decompose it into stokes parameters $I, Q, U, V$ with Pauli matrices $\sigma_{ab}^{(\alpha)}$ (here $\sigma_{ab}^{(0)}$ is the indentity matrix and these 4 matrices form a basis of the vector space of Hermitian $2 \times 2$

matrix):

$$\tilde{\mathcal{P}}_{ab} = E_a^* E_b = \frac{1}{2}\left[I\sigma_{ab}^{(0)} + U\sigma_{ab}^{(1)} + V\sigma_{ab}^{(2)} + Q\sigma_{ab}^{(3)}\right]. \tag{1.3}$$

In terms of electric field the Stokes parameter can be represented by

$$\begin{aligned} I &\equiv |E_1|^2 + |E_2|^2 \\ Q &\equiv |E_1|^2 - |E_2|^2 \\ U &\equiv E_1^* E_2 + E_2^* E_1 = 2\mathrm{Re}(E_1^* E_2) \\ V &\equiv 2\mathrm{Im}(E_1^* E_2). \end{aligned} \tag{1.4}$$

Here $I$ is the intensity of the electromagnetic wave, $Q$ and $U$ describe the linear part of the polarization whereas $V$ the circular one. (There is another convenient expression if using the real parts (projections) of the electric fields, see appendix A for the detail and the specific physical explanation on Stokes parameters.)

As we discussed in the Thomson scattering part, the circular polarization would not be produced. Therefore, in CMB research, scientists would only concern about the three stokes parameters $I, Q, U$ and in many occasions the intensity $I$ is replaced by the black-body temperature $T$ with a certain factor as indicated in (1.1).

Now we have the polarization tensor

$$\tilde{\mathcal{P}}_{ab} = E_a^* E_b = \frac{1}{2}\left[I\sigma_{ab}^{(0)} + U\sigma_{ab}^{(1)} + Q\sigma_{ab}^{(3)}\right]. \tag{1.5}$$

From this tensor we can extract out the polarization part which is a real symmetric traceless matrix

$$\mathcal{P}_{ab} = \frac{1}{2}\left[U\sigma_{ab}^{(1)} + Q\sigma_{ab}^{(3)}\right] = \frac{1}{2}\begin{bmatrix} Q & U \\ U & -Q \end{bmatrix}. \tag{1.6}$$

**Stokes parameters as a spinor**

The polarization part $\mathcal{P}_{ab}$ transforms as a spin-2 variable[16], see deduction details in appendix A. Using helicity basis $\boldsymbol{\epsilon}^{(\pm)} = \left(\boldsymbol{\epsilon}^{(1)} \pm i\boldsymbol{\epsilon}^{(2)}\right)$ we can define the following quantities

$$\begin{aligned} P &\equiv \mathcal{P}_{++} = 2\mathcal{P}^{ab}\boldsymbol{\epsilon}_a^{(+)}\boldsymbol{\epsilon}_b^{(+)} = Q + iU, \\ \bar{P} &\equiv \mathcal{P}_{--} = 2\mathcal{P}^{ab}\boldsymbol{\epsilon}_a^{(-)}\boldsymbol{\epsilon}_b^{(-)} = Q - iU. \end{aligned} \tag{1.7}$$

Here the meaning of spin-2 is more clear, because these two quantities transform as

$$(Q \pm iU)' = e^{\pm 2i\alpha}(Q \pm iU), \tag{1.8}$$

with a magnetic quantum number $\pm 2$.

We can see that $Q$ and $U$ are not rotational invariant, since they depend on the arbitrary choice of $\boldsymbol{\epsilon}^{(1)}$ and $\boldsymbol{\epsilon}^{(2)}$. Although normally the observations of the CMB are taken under the galactic coordinate system, we would like to extract invariant quantities from the rotation-dependent Stokes parameters to dig more deeply into the physics. This is done in the next item where the $Q$ and $U$ parameters are transformed into the E- and B-modes.

**From Stokes parameters to E-mode and B-mode**

We are going to introduce the spin weighted spherical harmonic functions ${}_sY_{\ell m}(\boldsymbol{n})$, which are the extension of the normal spherical harmonic functions $Y_{\ell m}(\boldsymbol{n}) = {}_0Y_{\ell m}(\boldsymbol{n})$. The spin weighted spherical harmonic functions change in this way:

$$ {}_sY_{\ell m}(\boldsymbol{n}) \Rightarrow e^{is\alpha}\, {}_sY_{\ell m}(\boldsymbol{n}), \tag{1.9} $$

and here we are going to consider only spin number 2.

On the full sky, the celestial shpere, considered as the scattering plane, the canonical basis $(\boldsymbol{e}_\theta \equiv \partial_\theta, \boldsymbol{e}_\phi \equiv \frac{1}{\sin\theta}\partial_\phi)$ which is defined on the tangent space of the sphere could not be well defined at both poles. Thus we choose helicity basis $\boldsymbol{e}^{\pm} = \frac{1}{\sqrt{2}}\left(\boldsymbol{e}_\theta \pm i\boldsymbol{e}_\phi\right)$, then our two familiar quantities can be expanded into

$$ (Q \pm iU)(\boldsymbol{n}) = \sum_{\ell=2}^{\infty}\sum_{m=-\ell}^{\ell} a_{lm}^{(\pm 2)}\, {}_sY_{\ell m}(\boldsymbol{n}), \tag{1.10} $$

where here we can split $a_{lm}^{(\pm 2)}$ into two parts

$$ a_{lm}^{(\pm 2)} = e_{lm} \pm ib_{lm}, \tag{1.11} $$

and

$$ \begin{aligned} e_{lm} &= \frac{1}{2}\left(a_{lm}^{(2)} + a_{lm}^{(-2)}\right) \\ b_{lm} &= \frac{-i}{2}\left(a_{lm}^{(2)} - a_{lm}^{(-2)}\right). \end{aligned} \tag{1.12} $$

Here we could have spin raising and lowering operators $\eth$ and $\eth^*$, an analogy to the ladder operator in quantum mechanics, which can act on the spin weighted spherical harmonic functions. To get the spin 2 weighted spherical harmonic functions back to spin 0, we need to lower the spin twice from 2 using $\eth^2$ or to raise the spin from -2 using $(\eth^*)^2$.

Acting on $Q \pm iU$, we will have

$$ \begin{aligned} (\eth^*)^2(Q+iU)(\boldsymbol{n}) &\propto \sum_{\ell=2}^{\infty}\sum_{m=-\ell}^{\ell} a_{lm}^{(+2)} Y_{\ell m}(\boldsymbol{n}) \\ \eth^2(Q-iU)(\boldsymbol{n}) &\propto \sum_{\ell=2}^{\infty}\sum_{m=-\ell}^{\ell} a_{lm}^{(-2)} Y_{\ell m}(\boldsymbol{n}), \end{aligned} \tag{1.13} $$

both with a factor $\sqrt{\frac{(l+2)!}{(l-2)!}}$.

Using this results, define two scalar quantities below,

$$ \begin{aligned} \mathcal{E}(\boldsymbol{n}) &= \sum_{\ell=2}^{\infty}\sum_{m=-\ell}^{\ell} e_{lm} Y_{\ell m}(\boldsymbol{n}) \\ \mathcal{B}(\boldsymbol{n}) &= \sum_{\ell=2}^{\infty}\sum_{m=-\ell}^{\ell} b_{lm} Y_{\ell m}(\boldsymbol{n}), \end{aligned} \tag{1.14} $$

they are scalar because $Y_{\ell m}(\boldsymbol{n})$ is a scalar, that is also the reason that we used lowering and raising operators.

$\mathcal{E}$ is like a gradient and $\mathcal{B}$ is like a curl, that is how they get their names, taking the analogy of the electric and magnetic field in electrodynamics. See appendix A for detail.

## 1.4 The Anisotropies

In order to explain the fluctuation in temperature and polarization maps of the CMB, we need to consider the fluctuation in the early universe, i.e., during the inflation period. We will see that inflation expanded the quantum fluctuation into a comparable level as a seed of today´s universe.

Inflation provides a physical mechanism by which several fundamental properties of our universe can be explained. However, it lacks a particle physics theory to sustain it, i.e., there is no particle in the Standard Model can become the candidate which responsible for the inflation, and its observational evidence is still quite weak.

In inflation theory, we believe there was a field call the inflaton driving the spacetime to expand extremely at the ultimate beginning of the universe after the Big Bang. The most common model is single-field slow-roll model. The kinematics can be found in appendix B.

The anisotropy of the CMB is studied in a statistical way rather than looking into every point carefully, because the perturbation is a quite stochastic mechanism and the latter method is therefore meaningless. We use angular power spectrum to express the anisotropy distribution.

#### Multipole expansion and angular power spectrum

We should know any scalar field $\Delta T(\vec{n})$ on a sphere can be expressed as a series of spherical harmonic multipoles, this is so-called multipole expansion:

$$\Delta T(\vec{n}) = \sum_{\ell} \sum_{m=-\ell}^{\ell} a_{\ell m} Y_{\ell m}(\vec{n}), \tag{1.15}$$

where the normalized spherical harmonic functions are

$$Y_{\ell,m}(\theta,\phi) = n_{\ell,m} P_{\ell,m}(\cos\theta) e^{im\phi}, \tag{1.16}$$

$P_{\ell,m}$ is the Legendre polynomials and $n_{\ell,m} = \sqrt{\frac{2\ell+1}{4\pi}\frac{(\ell-m)!}{(\ell+m)!}}$ is the normalization factor. We are familiar with these expressions since we have seen them when solving the Schrodinger equation of the Hydrogen atom.

The angular power spectrum is defined as following

$$C_\ell = \frac{1}{2\ell+1} \sum_{m=-\ell}^{\ell} |a_{\ell m}|^2 . \tag{1.17}$$

$C_\ell$ is a function of multipole $\ell$, denoting each multipole's contribution to the total fluctuations. We can regard it as a metaphor to the results of different frenquencies from the Fourier transformations, but instead of real frequencies we adapt the angular frequency $\ell$. Higher the multipole is, smaller the correspondent angle on the sky is, i.e., $\ell = 1$ correspond to dipole contribution, roughly 180 degree on the sky, $\ell = 10$ corresponds to roughly 10 degrees on the sky, $\ell = 100$ corresponds to roughly 1 degree on the sky[17]. Notice here we mean the size of a patch on the sky,

and notice the 'rough' correspondence, because there is no direct linkage between multipole and solid angle on the sky.

### 1.4.1 Perturbations

The perturbation happened in the inflation were two kinds, scalar perturbation (density perturbation) and tensor perturbation (Primordial Gravitational Waves, PGW). See appendix B to know how the perturbation is induced.

These two perturbations are related to the inflaton field potential $V$ and its time derivative $V'$, where here $H$ is the Hubble parameter and $M_{\mathrm{Pl}}$ is the Planck mass:

$$\begin{aligned} \Delta^2_{\mathcal{R}}(k)\frac{1}{8\pi^2}\frac{H^2}{M^2_{\mathrm{Pl}}} &= \frac{1}{12\pi^2}\frac{V^3}{M^6_{\mathrm{Pl}}(V')^2}, \\ \Delta^2_t(k) &= \frac{2}{\pi^2}\frac{H^2}{M^2_{\mathrm{Pl}}}. \end{aligned} \tag{1.18}$$

They can be expressed in power law with a reference $k_*$ and their corresponding amplitudes $A_s$ and $A_t$ and spectral indices $n_s$ and $n_t$ which are important in cosmological models.

$$\begin{aligned} \Delta^2_{\mathcal{R}}(k) &\equiv A_s\left(\frac{k}{k_*}\right)^{n_s-1}, \\ \Delta^2_t(k) &\equiv A_t\left(\frac{k}{k_*}\right)^{n_t}. \end{aligned} \tag{1.19}$$

The ratio between the amplitude of scalar perturbation and tensor perturbation, define a tensor-to-scalar ratio $r$ where $\epsilon$ the slow-roll parameter, relevant to $V$ and $V'$:

$$r \equiv \frac{\Delta^2_b}{\Delta^2_{\mathcal{R}}} = \frac{A_t}{A_s} = 16\epsilon. \tag{1.20}$$

As well as spectral indices, this tensor-to-scalar ratio can help us constrain the different cosmological models, e.g., Starobinsky's $f(R)$ gravity, one of them has a inflation with $r = \frac{12}{N^2}$ where $N$ is the e-fold in the inflation[18].

Inflation behaved like a magnifier enlarging the effects from primordial perturbations. The perturbations will affect the photon distribution and polarization at the LSS and then affected the CMB, see appendix B for detail.

## 1.5 E-modes and B-modes from the perturbations

The deduction in appendix B shows how the perturbations generate E and B-mode polarization patterns. In a word, we have E-mode polarization from both scalar perturbation and tensor perturbation but B-mode polarization only from tensor perturbation. Therefore, B-mode polarization is the imprint of the PGWB, and since PGWB is impossible to detect directly using GW observatories like LIGO, even LISA because it has an extremely long wavelength up to millions of lightyears, detecting B-mode polarization is the 'easiest', indirect way to observe PGWB. The existence of the B-mode is crucial to the correctness of the inflation theory and its strength, distribution and spectra, are important to modern cosmological models.

Today in 2020s, E-mode polarization has been observed but not the B-mode. Modern observation suggests a upper bound of $r$ as around 0.044[7] and theories suggest a possible lower bound of $r$ as around 0.001.

# Chapter 2

# Observational effects in the CMB polarization measurement

To reach the criterion to have the chance to observe the PGWB signal is not easy, not only because polarization only takes 10% of the total CMB[19], not to mention that B-mode polarization signal is much weaker than E-mode signal according to the theory, but also because of instrumental noises and the existence of systematic effects which need us to do the purging and cleaning. The foreground, or generally external effects include galactic foreground from synchrotron, dust, Bremsstrahlung emission and inverse Compton effect in our galaxy; weak-gravitational-lensing induced B-mode which turns E-mode into B-mode, sampling noises depending on the observation area fraction of the sky, and detector white noise (depending on the sensitivities of the detectors. Today the detector has reached to its quantum limit thanks to the development of manufacturing technology). Internal effects, which differ a lot from one configuration to another include beam imperfection, polarization angle mismatch, and pointing direction error. Collectively they are called calibration error. The reason is the hardness of precise calibrations.

For the galactic foreground, scientists did the observation in the different frequency bands to do the component separation. As for the signal from the weak lensing, scientists used lensing field profile to do the delensing.

In this work we are going to focus on the internal systematic effects, i.e., the calibration error, to see how much their influences are, covering the B-mode signal from the primordial gravitational wave.

First, it is hard to confine the polarimeters' position in a precision of half a degree relative to a known coordinate system, e.g., galactic coordinates. An unknown rotation will mix the E-mode and B-mode together and causes induced B-mode covering the original one. Second, the accurate pointing is an issue too, which collects the data that belongs to one of the points close to the designated point. An error of half a degree will cause strong noise covering the real signal. Third, beam imperfection. The beam profile of the telescope is normally irregular instead of a point function or a Gaussian function. Beam convolves with the map, reduces the resolution, but deconvolution can save us from blurring if the beam profile is well known and calibrated. However, the far-sidelobe response so weakly for us to calibrate in the laboratory, and there is no good-enough standard astronomical source in the sky. Therefore, we miss some information about the sidelobes, which are even though weak will collect strong signals from the foreground and cause noises covering B-mode signal.

We compared different future experiments including PICO, LiteBIRD, two telescopes of the Simons Observatory and two measurement configurations of CMB Stage-4, etc. We considered the noise power spectrums produced by different experiments with different parameter settings utilizing software simulations mainly

via HEALPix (Healpy), PySM and CAMB. We then evaluated their future prospective ability to discover the true B-mode CMB polarization signal from the primordial gravitational waves by giving an upper bound of the detectability on r. Besides, we provided suggestions about the calibration constraints on different configurations in order to reach the desired sensitivity and then have the discovery.

## 2.1 Foreground

### 2.1.1 Galactic foreground

In the microwave band, our galaxy emits a huge amount of radiation mainly via synchrotron ($< 100$ GHz), dust ($> 100$ GHz) and free-free Bremsstrahlung emission. We are unluckily sitting in the galaxy disk and one of the galaxy arm, whose star density is relatively high such that our view to the outside universe is blocked; but on the other hand, luckily we are at the edge of our galaxy, which allows us to barely see the counter-direction of the galaxy center. Contamination from the Sunyaev-Zel'dovich effect (100-300 GHz) should not be omitted too.

One way to remove the foreground is called component separation. We know the frequency dependent properties of different radiations, e.g., CMB follows Planck radiation law, synchrotron follows power law etc. Then we can ask for multiple-band observation to distinguish contributions from every kinds of sources.

In addition, normally physicists will apply a 'mask' onto the sky map before doing the harmonic analysis, avoiding the sky part with strongest galaxy-center radiation and extragalactic sources like M31. In these regions, it is nearly impossible to get true CMB radiation even if we apply the component separation.

### 2.1.2 Weak Lensing

Gravitational weak lensing (or cosmic shear) is an effect described by the general theory of relativity. In the contrary, this effect rarely produces the giant arcs and multiple images associated with strong gravitational lensing. A 3-D gravitational potential along the sight direction $\Phi$ will have a nonlinear effect on the CMB polarization, deflecting one point signal to the other with $\delta\theta = \nabla\Phi$[16]:

$$\begin{bmatrix} T \\ Q \\ U \end{bmatrix}_{\text{obs}} (\boldsymbol{\theta}) = \begin{bmatrix} T \\ Q \\ U \end{bmatrix}_{\text{ls}} (\boldsymbol{\theta} + \delta\boldsymbol{\theta}) \simeq \begin{bmatrix} T \\ Q \\ U \end{bmatrix}_{\text{ls}} (\boldsymbol{\theta}) + \delta\boldsymbol{\theta} \cdot \nabla \begin{bmatrix} T \\ Q \\ U \end{bmatrix}_{\text{ls}} (\boldsymbol{\theta}), \tag{2.1}$$

and mixing B-mode with E-mode:

$$C_\ell^{\text{BB}} = \int \frac{\mathrm{d}^2 \boldsymbol{l}_1}{(2\pi)^2} \left[\ell_1 \cdot (\ell - \ell_1)\right]^2 \sin^2 2\varphi_{\ell_1} C_{|\ell-\ell_1|}^{\Phi\Phi} C_{\ell_1}^{\text{EE}}. \tag{2.2}$$

However, We need a delensing profile at map-level rather than at spectrum level just like (2.2) because the lensing sources are not isotropic and homogeneous in the sky, delensing profile at every single point is unique, which raises requirements of a prior knowledge about the lensing field $\Phi$.

## 2.2 Systematic effects

In the sections above, we talked external effects from the foreground, which is global and does vary from one instrument to another. Meanwhile, there are internal effects comes from the different sensitivities of the instrument and the residual signals come from the calibration that is highly depending on the instrument configurations and the calibration processes.

### 2.2.1 Detector Noises and sampling, sensitivities

Now a days, the detectors have already reached their quantum limit thanks to the state-of-art superconducting technologies and cooling methods. The sensitivity of a detector in a unit area can no longer be improved significantly, so the only way to increase the sensitivity is increasing the number of detectors (arrays) or enlarging the area of the focal plane where we put the detector arrays. On the other hand, systematics related to the themal fluctuations at the focal plane, that directly impact the gain of the detectors, need to be well under control, implying a control of the temperature at the mili-kelvin level.

Another source of uncertainty comes from the sampling area. The typical sampling noise is considered to be white, i.e., same power at any $\ell$ with a typical strength around several $\mu\text{K} \cdot \text{arcmin}$ in terms of the standard deviation. For a given noise per angular scale, the larger the observed area, the smaller the uncertainty in the B-mode power spectrum and therefore in the $r$ parameter. On the other hand, the antenna resolution plays also an important role. For the angular scales where the primordial B-mode signal is relevant, above 1 degree, small aperture telescopes with diameters smaller than a meter are better adapted than large aperture ones. The major resolution of the latter, typically of several arcminutes, results in a major part of the observational effort concentrated in sub-degree scales[1].

In relation to ground-based versus space-based telescopes, it is clear that space-based telescopes have the advantage of not having the atmosphere that absorbs and emits radiation in the microwave range. Due to this, the efficiency of 1 detector in space is equivalent to roughly 100 detectors form the ground. On the other hand, space telescopes have very strong physical limitations, in particular in relation to the size of the focal plane.

These effects can be sum over as an factor generally called 'sensitivity', or just 'noise level' in the unit of $\mu\text{K} \cdot \text{arcmin}$ which can be regarded as an fixed value and it acts like a white noise with a constant power in the power spectrum.

### 2.2.2 Sky coverage

From one instrument to another, the fraction of the sky that is able to be observed $f_{sky}$ is different depending on whether the instrument is in the space or ground-based or carried by the balloon.

The sky coverage is a problem for the ground-based telescopes because the visible sky is depending on the observatories' latitude while the space telescopes do not worry. In this case, polar observatories worry more than those located in low latitude. For example, telescopes in Antarctica, e.g., the Simons Observatory never see the sky in northern celestial hemisphere while Stage-4 in Atacama, Chile have the

[1] In terms of multipoles, the B-mode spectrum peaks at both the recombination era and reionization era between $2 < \ell < 200$, so this multipole range is vital for detecting B-modes.

ability to observe most of the northern celestial hemisphere and all of the southern celestial hemisphere.

The sky coverage of the space telescope is 100% in principle. However, due to strong emission from the galactic plane and from some extragalactic source like M31 it's impossible to get any meaningful CMB signal from those area. Therefore the available sky is reduced to a typical ratio 60% and possibly 80% in the future. Meanwhile, the sky coverage is also depending on the observational strategy. For example, Stage-4 ultra-deep measurement. In order to have the high fidelity and low contamination it observes only 3% of the sky where the foreground is exceptional low[20].

This observation incompleteness and the harmonic analysis on a incomplete celestial sphere will cause information loss and thus brings the noises.

### Polarization angle mismatch

One factor is polarization angle mismatch. We already know that Stokes parameters $Q$ and $U$ can transform like a spin-2 tensor if we tilt the observation field of view. The point is , it is hard to firmly fix the focal plane reference frame. With a small angular error between the polarimeter and the detector, the analysis will produce a comparable amount of false B-mode signal.

The calibration of the polarization angle suffers from the ambient environment change and the telescope structure instability. For example, the space telescope which is calibrated on the ground will go through the temperature change, air pressure change and the vibration during the transportation and the launch, etc.

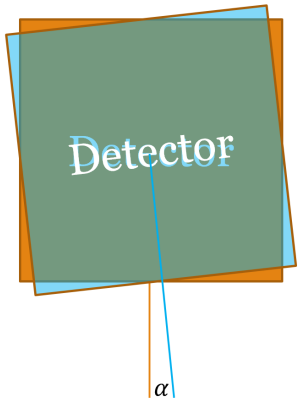


FIGURE 2.1: Illustration of the polarization angle mismatch. This angle mismatch can happen between the detectors and polarimeters, or between the telescope and the reference frame.

### Random Pointing

Another factor is random pointing, similar to polarization angle mismatch, the pointing direction control is too coarse to produce a clean, true polarization map.

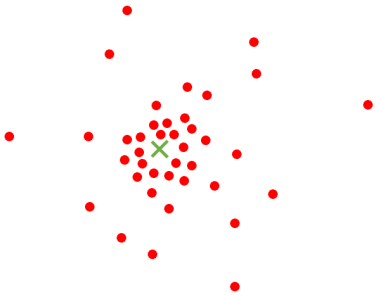

FIGURE 2.2: An illustration of one of the possibility distribution of the real pointing direction (in red dots) while we think the instrument is pointing to the green-cross direction. It's more likely to have a small radial error rather than a big difference. In practice later, we will consider a absolute Gaussian distribution for the radial error.

One of the reasons of the random pointing can be the bad precision and accuracy in the mechanical structure or the error in the positioning feedback system.

Besides, if the resolution (central beam FWHM) of the telescope is not good enough, pointing error will be induced after the pointing calibration using the astronomical object on the sky.

Another reason could be the focal plane misalignment, leading to differential pointing errors between the detectors[21].

### 2.2.3 Beam calibration imperfection

Another factor is the unclear beam profile. The beam is not a point function even for a perfect telescope whose beam profile is a gaussian function. Normally microwave antennas not only have responses at the direction of pointing, but also have bizzare-shaped low-response sidelobes coming from the structure of the telescope, e.g., baffles, spanning a wide angle between the pointing direction and collecting unwanted signals from sides, especially the foreground signal, see figure 2.3 which is way more stronger than the CMB. Sidelobes with large angle between the central beam are called far-sidelobes.

Although the beam convolves with the map, we can do the deconvolution to achieve the original map if we know the explicit beam profile. However, weak sidelobes below a certain response level have not been calibrated or been unable to calibrate under current technology limitations.

For instance, to have a laboratory big enough containing the whole large structure of the instrument and having a stable, required environment for the calibration, e.g., a stable low temperature environment down to several Kelvin, is extremely expensive time-consuming. For those space telescopes, it is possible to do the calibration using celestial objects, e.g., Taurus A (the radio source corresponds to the Crab Nebula M1, one of the best calibration source on the sky) or planets. However, the lights from those objects are not fully polarized and they are actually fluctuating and thus limit our calibration. For example, the limit is typically -50 dB to the peak amplitude for Planck calibration using the signal from the Jupiter[22, 23],

So it's clear that the deconvolution with the part-unknown beam will introduce spurious signal.

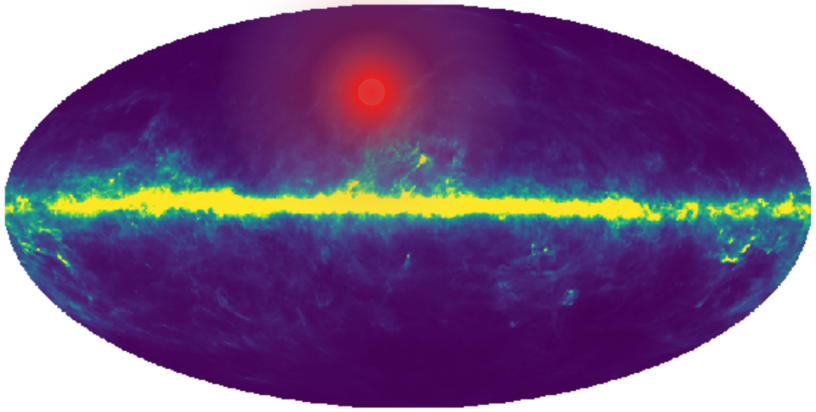

FIGURE 2.3: Red beam convolves with the foreground map. The redness exaggeratedly denotes the beam responses. We can see although the far-sidelobes have weak response but they collect the strongest signal from the galactic disk even if the central beam is pointing far away from the galactic disk.

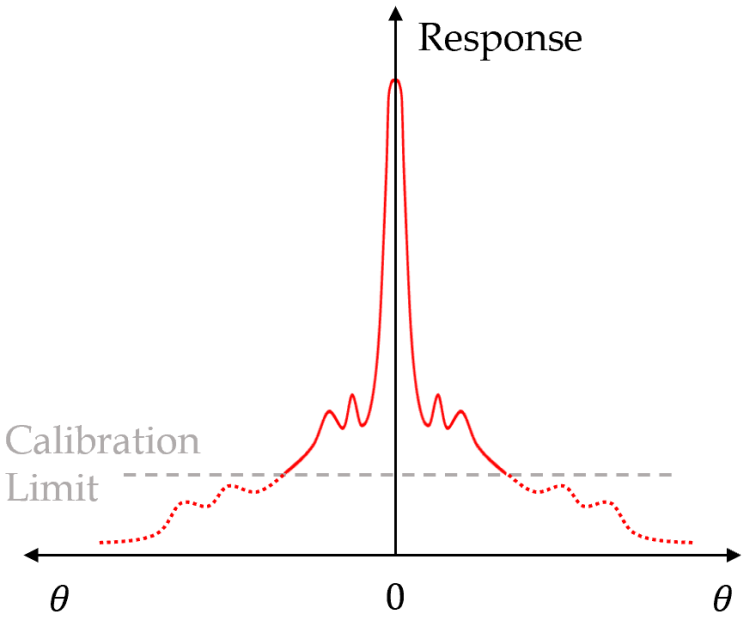


FIGURE 2.4: A circular beam with strong central beam, weaker sidelobes and very weak uncalibrated far-sidelobes.

This study will focus on the above three systematic effects of the following 4 future experiments that will carry on the exploration of the B-mode CMB signal: LiteBIRD, Stage-4, the Simons observatory, PICO.

## 2.3 Experiments

### 2.3.1 LiteBIRD

LiteBIRD (Lite (Light) satellite for the studies of B-mode polarization and Infation from cosmic background Radiation Detection) aims to detect signatures of these PGWB. LiteBIRD is focused on this point: targeting both the recombination era with the multipole moment $\ell$ between 11 and 200 and the reionization era with $\ell$ between 2 and 10, optimizing the angular resolution. The other important concepts of this satellite are a warm launch without the requirements of heavy vessels/tanks and use of multichroic detectors for the effective exploitation of finite focal-plane areas. Advantages of measurements from space are being free from atmospheric effects, providing high sensitivity, stability with less systematic uncertainties, and no restrictions on observing band selection. Space measurements also give no pickup from the ground. The Sun–Earth L2 point has been selected, since the Sun, the Earth, and the Moon are all located in almost direction, which makes it easier to avoid facing them in terms of optical and thermal aspects. Care should be taken, however, on cosmic ray effects because the satellite is more directly exposed to them. Sky observations are planned for 3 years: The presently guaranteed cooling-chain lifetime is 3.5 years, in which 0.5 year is assigned to the transitional period to the normal observation phase on course to L2.[24]

### 2.3.2 Stage-4

The next generation "Stage-4" ground-based cosmic microwave background (CMB) experiment, CMB-S4, consisting of dedicated small-aperture (0.55-meter) and large-aperture (6-meter) telescopes equipped with highly sensitive superconducting cameras operating at the South Pole, the high Chilean Atacama plateau, and possibly northern hemisphere sites. S4 will be designed to cross critical thresholds in testing inflation and is intended to be the definitive ground-based CMB project. CMB-S4 is the logical successor to the Stage-3 CMB projects which will operate over the next few years. The sensitivity and fidelity of the multiple band foreground measurements needed to realize the goals of S4 will be provided by S4 itself, at frequencies just below and above those of the main CMB channels. [20][25]

#### Deep and wide measurement

The Deep and wide measurement will take two large-aperture telescopes covering around 60% of the sky with 240000 detectors.

#### Ultra-deep measurement

The Ultra-deep measurement will take two small-aperture telescopes with 150000 detectors observing a small portion of the sky (3%) centers at RA=0h, Dec=-45deg and a large-aperture telescope for delesing purpose with 120000 detectors.

### 2.3.3 Simons Observatory

The Simons Observatory (SO) is a new cosmic microwave background experiment aimed at characterizing the primordial perturbations and is being built on Cerro Toco in Chile, due to begin observations in the early 2020s. SO will measure the temperature and polarization anisotropy of the cosmic microwave background in six frequency bands. The initial configuration of SO will have three small-aperture 0.5-m telescopes and one large-aperture 6-m telescope, with a total of 60,000 cryogenic bolometers. [26]

#### Small Aperture Telescopes

The small aperture telescopes will target the largest angular scales observable from Chile, mapping $\approx$ 10% of the sky to a white noise level of 2 $^{-}$K arcmin in combined 93 and 145 GHz bands, to measure the primordial tensor-to-scalar ratio, r, at a target level of $\sigma_r = 0.003$.

#### Large Aperture Telescope

The large aperture telescope will map $\approx$ 40% of the sky at arcmin angular resolution to an expected white noise level of 6 $^{-}$K arcmin in combined 93 and 145 GHz bands, overlapping with the majority of the Large Synoptic Survey Telescope sky region and partially with the Dark Energy Spectroscopic Instrument. With up to an order of magnitude lower polarization noise than maps from the Planck satellite, the high-resolution sky maps will constrain cosmological parameters derived from the damping tail, gravitational lensing of the microwave background, the primordial bi-spectrum, and the thermal and kinematic Sunyaev-Zel'dovich effects, and will aid in delensing the large-angle polarization signal to measure the tensor-to-scalar ratio.

### 2.3.4 PICO

The Probe of Inflation and Cosmic Origins (PICO) is a NASA-funded study of a Probe-class mission concept, an imaging polarimeter that will scan the sky for 5 years in 21 frequency bands spread between 21 and 799 GHz. It will produce full-sky surveys of intensity and polarization with a final combined-map noise level of 0.87 micro-Kelvin arcmin for the required specifications, equivalent to 3300 Planck missions, and with our current best-estimate would have a noise level of 0.61 micro-Kelvin arcmin (6400 Planck missions). PICO will either determine the energy scale of inflation by detecting the tensor to scalar ratio at a level $r = 5 \times 10^{-4} (5\sigma)$, or will rule out with more than $5\sigma$ all inflation models for which the characteristic scale in the potential is the Planck scale. [27]

#### Comparison

The basic configuration of the instruments are listed in table 2.1.

The central beam resolution is highly depending on the working frequency. Higher the frequency is, finer the resolution is. Following the Rayleigh criterion of the ideal angular resolution of a circular aperture $1.22\frac{\lambda}{D}$ where $\lambda$ is the wavelength and $D$ is the fixed aperture size. We picked the most representative resolution around 100GHz for LiteBIRD and for others around 150GHz.

The sky coverage for LiteBIRD and PICO is conservative. In a decades, it can potentially reach 80% depending on the component separation.

TABLE 2.1: Instrument configurations

| Instruments | Central Beam FWHM (′) | Total Sensitivity $\sigma_n$ ($\mu$K · arcmin) | Sky Coverage $f_{sky}$ |
|---|---|---|---|
| LiteBIRD[28] | 30 @100GHz | 2 | 60% |
| CMB-S4 DW[20] | 1.4 @145GHz | 2.8 @145GHz | 60% |
| CMB-S4 UD[20] | 1.5 @145GHz | 0.96 @145GHz | 3% |
| SO LAT[26] | 1.4 @145GHz | 6 | 40% |
| SO SAT[26] | 17 @145GHz | 2 | 10% |
| PICO[27] | 6.2 @155GHz | 0.61 | 60% |

## 2.4 Quantification of the systematic effects (Detectability)

### 2.4.1 Uncertainty (error) in $r$

When harmonic analysis is performed on the sky, we assumed that every harmonic coefficient $a_{\ell m}$ drawn from the Gaussian distribution with a variance $C_\ell = \langle |a_{\ell m}|^2 \rangle$. We can have an estimator which is the sum of these independent Gaussian variables' square $\hat{C}_\ell = \sum_{m=-\ell}^{\ell} \frac{|a_{\ell m}|^2}{2\ell+1}$ with a root variance $\left(\frac{2}{2\ell+1}\right)^{\frac{1}{2}} C_\ell$.

All the defects and noises will provide us a lower bound to detect the crucial $r$. Each measured multipole moment gives an estimator $\hat{r}_\ell$. If we use the hypothetical PGWB power spectrum with a strength $r = 0.1$ as a criterion, and from the observation $C_\ell^{\rm obs}$ the estimator will be

$$\hat{r}_\ell = 0.1 \times \frac{C_\ell^{\rm obs} - \sum_i C_\ell^{\rm i}}{C_\ell^{\rm PGWB}(r = 0.1)}. \tag{2.3}$$

Here the index $i$ denotes different kinds of noise, e.g., foreground, lensing, etc.

Summing over all the estimators with inverse-variance weighting, under the null hypothesis $r = 0$, the root variance of this minimum-variance estimator of $r$ will be[16]:

$$\sigma_r \simeq \frac{0.1}{\sqrt{f_{\rm sky}}} \left\{ \sum_{\ell=\ell_{\rm min}}^{\ell_{\rm max}} \frac{(2\ell+1)}{2} \left[ \frac{C_\ell^{\rm PGWB}(r = 0.1)}{\sum_i C_\ell^{\rm i}} \right]^2 \right\}^{-1/2}. \tag{2.4}$$

### 2.4.2 Bias in $r$

In addition to the statistical uncertainty produced by the residuals of the different systematic effects, another important quantity to consider is the bias of the estimator. This is what has been done in another paper for the case of the polarization angle mismatch[29] for the case of LiteBIRD. From the results obtained in that paper it seems that the bias could introduce errors comparable or larger than the statistical uncertainties. Therefore, although this quantity is not used in the present work, it should be considered for obtaining more robust requirements not only in the polarization angle but also in the other systematics.

# Chapter 3

# Methodologies

## 3.1 Software

Most of the operations were performed in Python 3. All the codes are piled in jupyter notebooks and have already been uploaded onto GitHub *https://github.com/skycattmll/Jun-Yan_Zhang_TFM_codes*.

### Packages

The packages mainly used were Numpy [1] [30] for data in array-like forms and Matplotlib[2][31] for data plotting.

### 3.1.1 Analysis on the sky

#### Pixelization

We use package healpy and HEALPix, an acronym of Hierarchical Equal Area isoLatitude Pixelization to do the harmonic analysis[3][32, 33]. Healpy can subdivide the whole sphere into $12N_{side}^2$ equal pixels where $N_{side}$ is the resolution parameter which takes the form of non-negative-interger powers of 2. In our work, limited by the computer's computational capability, we set $N_{side} = 512$, corresponding to an angle $\approx$ 6.87 arcmin[34] to fulfill the requirement of the resolution as much as possible. This $N_{side}$ corresponds to a maximum multipole $\ell_{max} = 3N_{side} - 1 = 1535$.

#### Harmonic analysis

The main functions used in the harmonic analysis are *healpy.sphtfunc.anafast* to provide T,E,B power spectra and TE,TB,EB cross-spectra by giving T,Q,U maps and *healpy.sphtfunc.synfast* to generate random T,Q,U maps inversely by giving power spectra and their correlations.

The power spectrum is defined in equation 1.17 and sometimes cosmologists like to use a equivalent quantity

$$D_\ell = \frac{\ell(\ell+1)C_\ell}{2\pi}, \tag{3.1}$$

and both of them have unit in Kelvin square $K^2$ (due to CMB fluctuation level, micro-Kelvin square $\mu K^2$ is more commonly used). Also some scientists takes the square root on $D_\ell$ with or without the $2\pi$ denominator inside the root.

[1] https://numpy.org/
[2] https://matplotlib.org/stable/index.html
[3] http://healpix.sourceforge.net

**View the maps**

We use Mollweide projection, an equal-area, pseudocylindrical map projection to visualize the whole sky maps with the function code *healpy.visufunc.mollview*.

### 3.1.2 CMB power spectrum simulation

The CMB power spectrum simulation is achieved using package CAMB, an acronym of Code for Anisotropies in the Microwave Background[4][35][36].

The parameter setting used Planck 2018 results, the same as those in[37], obtained from Planck 2018 latest results[38]. The parameters in an *.ini* file can be dowloaded from Planck Legacy Archive[5][39].

The parameters are stored in an *.ini* file and we can use *cp = camb.read_ini( 'planck_2018.ini')* for example, to read them out as 'cp'. The power spectra, named 'powers' for instance, can be generate by using the code *powers = camb.get_results(cp). get_cmb_power_spectra( cp, CMB_unit='muK')* with the unit of micro-Kelvin. The 'powers' has the following 6 directories:'total', 'unlensed_scalar', 'unlensed_total', 'lensed_scalar', 'tensor', 'lens_potential'. The unlensed CMB spectra (T,E,B, and correlations TE,TB,EB) with zero primordial B-mode is stored in the directory titled 'unlensed_scalar' and the lensed spectra (expected spectra from the observation) is stored in the directory titled 'total'.

By setting the initial parameter 'inflation_params' using *inflation_params = initialpower.InitialPowerLaw().set_params( r=0.044)*, we can generate parameters with arbitrary values of tensor-to-scalar ratio $r$, $r = 0.044$ for example. Then the power spectra 'powers_i' with a maximum multipole $\ell_{max}$ can be obtained using *powers_i = camb.get_transfer_functions(cp).power_spectra_from_transfer (inflation_params). get_unlensed_total_cls ($\ell_{max}$, CMB_unit ='muK')*. The most important PGWB B-mode spectrum $C_\ell^{PGWB}$ is the third column of 'powers_i' by default.

### 3.1.3 Sky simulation

The map-level whole sky simulation, including CMB, dust, synchrotron etc. is achieved using package PySM, an acronym of the Python Sky Model[6][40].

The code for getting sky map called 'sky' for example, is *sky=pysm3.Sky(nside=512, preset_strings=["d1", "s1", "c1"])*, and to get the emission in a certain frequency, for example 100GHz we used the function *sky.get_emission(100 * u.GHz)*. Here the dust and sychrotron emissions has the *preset_strings* as *d1* and *s1* and the CMB is *c1*:

- *d1*: Thermal dust is modelled as a single-component modified black body. We use dust templates for emission at 545 GHz in intensity and 353 GHz in polarisation from the Planck-2015 analysis, and scale these to different frequencies with a modified black body spectrum using the spatially varying temperature and spectral index obtained from the Planck data using the Commander code[41].

- *s1*: Power law scaling is used for the synchrotron emission, with a spatially varying spectral index. The emission templates are the Haslam 408 MHz, 57′ resolution data reprocessed by Remazeilles et al 2015 MNRAS 451, 4311, and the WMAP 9-year 23 GHz Q/U maps[42]. The polarization maps have been

[4] https://camb.info/
[5] http://pla.esac.esa.int/pla/#cosmology
[6] https://pysm3.readthedocs.io/en/latest/

smoothed with a Gaussian kernel of FWHM 5 degrees and had small scales added. The intensity template has had small scales added straight to the template. The details of the small scale procedure is outlined in the accompanying paper. The spectral index map was derived using a combination of the Haslam 408 MHz data and WMAP 23 GHz 7-year data[43]. The same scaling is used for intensity and polarization. This is the same prescription as used in the Planck Sky Model's v1.7.8 'power law' option[44], but with the Haslam map updated to the Remazeilles version. A 'curved power law' model is also supported with a single isotropic curvature index. The amplitude of this curvature is taken from[45].

- *c1*: A lensed CMB realisation is computed using Taylens, a code to compute a lensed CMB realisation using nearest-neighbour Taylor interpolation[46]. This code takes, as an input, a set of unlensed Cl's generated using CAMB.

Later, when we refer to the galactic foreground map, we are talking about the map mixed with *d1* and *s1*. The free-free Bremsstrahlung emission (*f1*) is ignored because intrinsically Bremsstrahlung radiation is unpolarized[47] and even if it is partially polarized by Thomson scattering within the HII region, it is not expected to polarize the emission by more than 10%[48]. We also negleted the AME (Anomalous Microwave Emission *a1* or *a2*) were not considered, because the polarization only account for little in AME (e.g., less than 0.22% at 41GHz)[49].

**Temperature conversion**

Normally the sky map *map* we get is not the CMB temperature but the antenna temperature. We must do the conversion using the function *map.to(u.uK_CMB, equivalencies = u.cmb_equivalencies( 100*u.GHz))*. The relationship between two temperatures is stated as follows:

In observation, instead of using the brightness $B$ in the unit of Jansky or equivalently erg $\mathrm{cm}^{-2}\mathrm{s}^{-1}\mathrm{Hz}^{-1}$, the antenna temperature or brightness temperature under the Planck unit system is

$$T_{ant} = \frac{B}{2\nu^2} = 2\pi\nu f. \tag{3.2}$$

It has the unit of Kelvin. However, the black body temperature of the CMB is different which has been shown in equation (1.1).

Since we know the zeroth (unperturbative) photon distribution function of the CMB is Bose-Einstein distribution with zero chemical potential, as a function of momentum $p$ and temperature $T$:

$$f^{(0)} = \frac{1}{e^{\frac{p}{T}-1}}, \tag{3.3}$$

the antenna temperature has the following relationship with the CMB isotropic temperature[8]:

$$\frac{T_{ant}}{T} = \frac{\frac{2\pi\nu}{T}}{e^{\frac{2\pi\nu}{T}}-1} = \frac{x}{e^x-1}, \tag{3.4}$$

where $x = \frac{2\pi\nu}{T}$.

With perturbations the distribution fuction can be expanded into the first order with temperature fluctuation $\Theta = \frac{\Delta T}{T}$, which is a function of photo distribution $\vec{x}$

(inhomogeneity), propagation direction $\hat{p}$ (anisotropy) and time $t$:

$$f \simeq f^{(0)} - p\frac{\partial f^{(0)}}{\partial p}\Theta. \tag{3.5}$$

With this, the temperature relation would be

$$\frac{T_{ant}}{T} = \frac{x}{e^x - 1} + \Theta\frac{x^2 e^x}{(e^x - 1)^2}. \tag{3.6}$$

Neglecting the first term, with which we are indiffrent,

$$\frac{T_{ant}}{T} = \Theta\frac{x^2 e^x}{(e^x - 1)^2} = \Theta W^{cmb}(x). \tag{3.7}$$

$W(x)$ is the shape vector. For different components, e.g. CMB, foregrounds it has different forms. Explicitly for the CMB, $W^{cmb}(x) = \Theta\frac{x^2 e^x}{(e^x-1)^2}$.

### 3.1.4 Beam convolution

Antenna beam $b$ convolves with the map and blurs our view. The fine details will be smeared out. At the power-spectrum level, the beam suppresses the moments at high multipoles.

Consider a circular beam, it is convenient to only discuss the beam's cross-section. Later, the 'beam' or 'beam profile' are referred to its cross-section.

Function *healpy.sphtfunc.beam2bl(b(θ), θ)* will turn the beam profile $b(\theta)$ in real space into beam window function $b(\ell)$ in harmonic space. The algorithm is simply

$$b_{\ell m} = \int d\mathbf{r} b(\mathbf{r}) Y^*_{\ell m}(\mathbf{r}) \tag{3.8}$$

and generally for a circular beam, which has axial symmetry

$$\begin{aligned} b(\ell) &= b_{\ell 0}\sqrt{\frac{4\pi}{2\ell + 1}} \\ &= \int b(\theta) P_\ell(\theta) \sin(\theta) d\theta 2\pi. \end{aligned} \tag{3.9}$$

#### Map-level convolution

In general at map-level, function *healpy.sphtfunc.smoothing(map, beam_window=bl)* allows us to do the convolution between the sky map *map* and *bl*, the beam profile $b(\ell)$ in terms of multipoles.

#### Ideal beam

In the case that the beam $b$ is ideal, i.e., a circular symmetric beam profile with a perfect Gaussian cross-section $b(\theta) \propto e^{-\frac{\theta^2}{2\sigma^2}}$ with the standard deviation of the Gaussian beam $\sigma$, we can directly using

$$a'_{\ell m} = Ant(\ell) a_{\ell m} = e^{-\frac{\ell(\ell+1)\sigma^2}{2}} a_{\ell m}, \tag{3.10}$$

where the function $Ant(\ell) = e^{-\frac{\ell(\ell+1)\sigma^2}{2}}$ is suppressing the power at high multipoles. The power spectrum will become

$$C'_\ell = Ant^2(\ell)C_\ell = e^{-\ell(\ell+1)\sigma^2}C_\ell. \tag{3.11}$$

For a Gaussian function, the relation between its standard deviation $\sigma$ and its FWHM is

$$\sigma = \frac{\text{FWHM}}{2\sqrt{2\log 2}}. \tag{3.12}$$

If the beam is not ideal, or the anisotropies are not evenly distributed on the sky, e.g., the foregrounds, it is necessary to do the beam convolution at the map-level in the way we have discussed.

### 3.1.5 Masks

We can apply the mask onto the sky map by directly multiply the mask map with the sky map. The mask should be an apodized map which means it takes the value from 0 to 1 smoothly. 0 value means that pixel is completely masked and 1 value means that pixel is in the mask window.

#### Mask for LiteBIRD, CMB-S4 DW, SO LAT, and PICO

For LiteBIRD, CMB-S4 DW, SO SAT, and PICO, since they all have large sky coverage, we generally took the 2 degree apodized galactic-plane mask map provided by Planck Legacy Archive[7][50] as shown in figure 3.1. Its completely masked area takes the ratio of 40.79% (sky coverage 59.21%), and if we consider the apodization the sky coverage would be around 60%.

Besides, the function *healpy.ud_grade()* is used to turn the mask map into the map with $N_{side} = 512$.

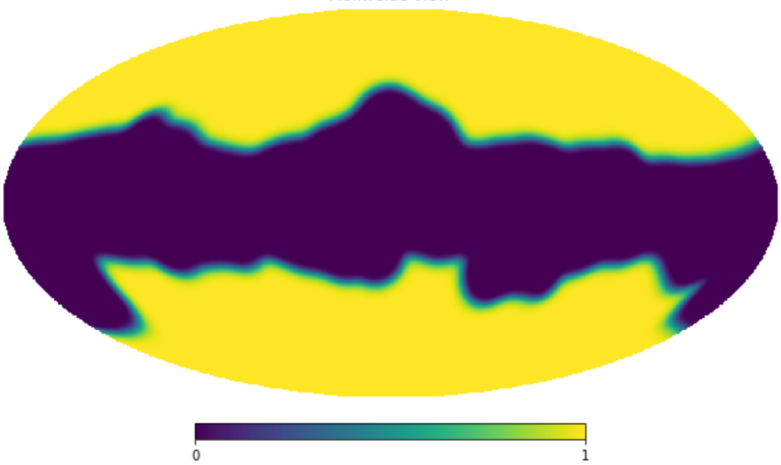


FIGURE 3.1: Planck's galactic plane mask that we applied

#### Mask for CMB-S4 UD measurement

Since ultra-deep measurement will pointing at a specific small region on the sky with minimum foregrounds, we should not use the previous Planck mask. According

[7] http://pla.esac.esa.int/pla/#cosmology

to the description of the ultra-deep measurement[8][51], an apodized circular mask centering at RA=0h, Dec=$-45^\circ$ with the default being flat to radius $\gamma = 12^\circ$ and then rolling to zero as cosine squared over an additional $15^\circ$ is used. This results in an effective sky coverage of 3%.

The angular distance $\gamma$ between each pixel on the sky with the celestial coordinates $(a, \delta)$ and the center point $(0^\circ, -45^\circ)$ can be obtained using the law of cosines

$$\gamma = \cos^{-1}\left[\sin(\delta)\sin(-45^\circ) + \cos(\delta)\cos(-45^\circ)\cos(a - 0^\circ)\right]. \tag{3.13}$$

Figure 3.2 shows the mask in relatively in equatorial coordinates and galactic coordinates after applying the code *healpy.rotator.Rotator(coord=['C', 'G'])*, and no need to say the mask definitely screens almost all the emission from the galactic plane.

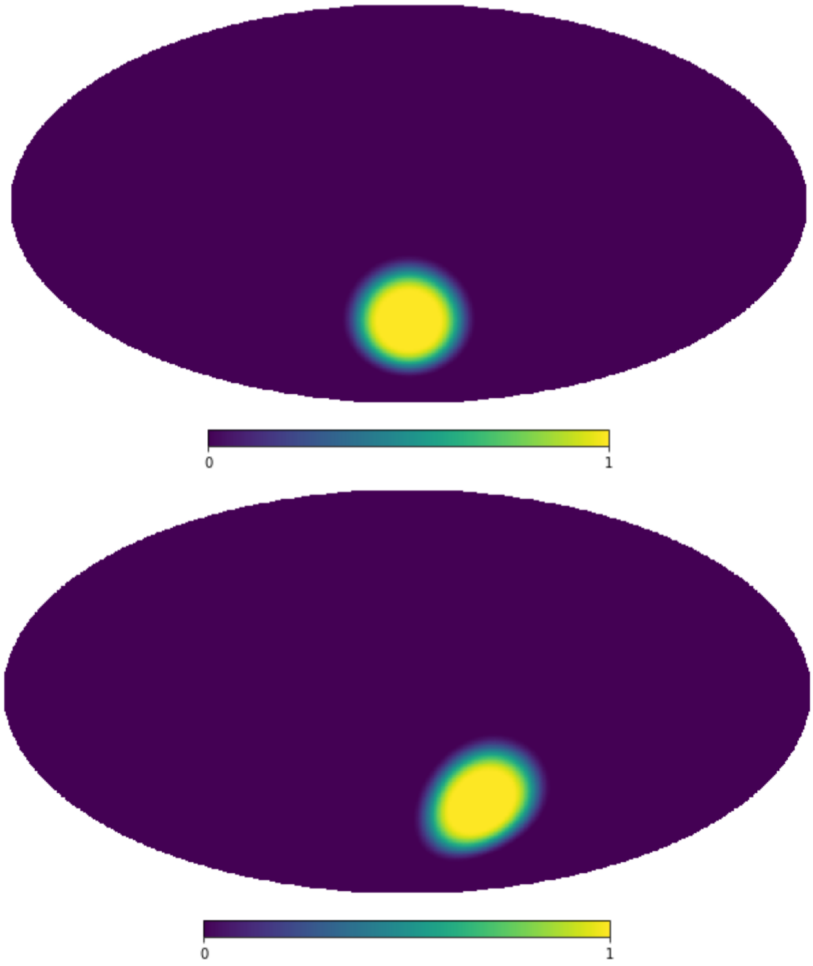


FIGURE 3.2: CMB-S4 ultra-deep measurement mask in the celestial equatorial coordinates (above) and galactic coordinates (below) with sky coverage 3%. The center locates at RA 0h and Dec $-45^\circ$, $12^\circ$ radius and a $15^\circ$ apodization region from 1 to 0 following a $\cos^2$ law. This the cleanest part on the sky if we compared it with the foreground maps.

[8] https://cmb-s4.uchicago.edu/wiki/index.php/Sky_masks_for_simulations

#### Mask for SO SAT

We would like to adapt the similar mask configuration of ultra-deep measurement to SAT, but only change the sky coverage from 3% to 10%, i.e., the angular radius and the size of the apodizing region should be enlarged $\sqrt{\frac{10}{3}}$ times . The mask in galactic coordinates would look like figure 3.3.

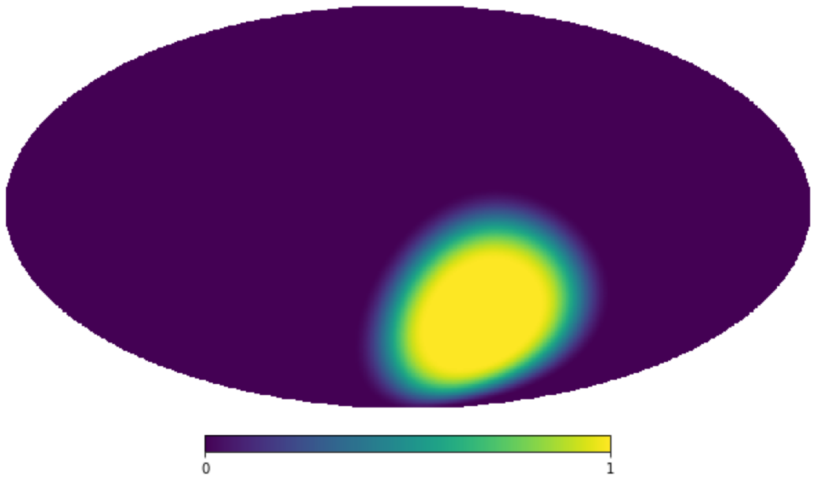


FIGURE 3.3: Small Aperture Telescope mask in the galactic coordinates with sky coverage 10%.

#### Influence of the mask in harmonic analysis

The mask only gives a fraction of the sky. The harmonic analysis on a fraction of sky will give a weaker power spectra. The equivalent whole sky power spectra would be $1/f_{sky}$ stronger if we consider the whole sky succeeds the properties of that fraction of the sky. Harmonic analysis on an incomplete sphere will also introduce correlations which we will not consider in our work.

### 3.1.6 Function smoothing

The power spectrum generating from the simulated map are normally jaggled due to numerical noises in the Fourier analysis. The same problem happens when doing the transformation of the beam profile from the real space to the harmonic space in the following section 3.3.2. We can use *scipy.signal.medfilt ()* function to apply a median filter on the curve. It can be regarded as a low-pass filter which preserves the general picture of the curve. The parameter *kernel_size* is odd and depending on the size of the bumps on the curve.

## 3.2 Foreground construction

When we start to talking about the influence of the factors on the estimation in $r$, we need to think about the foregrounds.

### 3.2.1 Galactic foreground

1 percent cleanest region on the sky have a power spectrum at 100GHz[52]

$$C_\ell^{clean} \approx 1.5 \times 10^{-2} \ell^{-2.29}. \tag{3.14}$$

Different experiments have different ability to remove the foregrounds. This ability is described by a factor $R_F$ in a range from 0.001 to 0.5 depending on how well the component separation can be performed. In principle, more frequency bands there are, better the component separation can be. Then we assume the galactic foreground has less influence to the observation with a power spectrum

$$C_\ell^{gal} = Ant(\ell) R_F C_\ell^{clean}. \tag{3.15}$$

For different experiments, $R_F$ are listed in table 3.1 below.

### 3.2.2 Weak Lensing

We took a power spectrum of the total B-mode from CAMB as $C_\ell^{lensing}$ which is the second row from the 'total' directories of the power spectra *powers['total'][:,2]*, see section 3.1.2. We assumed the PGWB is negligible compared to the lensed B-mode, that is meaning the total B-mode is the lensed B-mode approximately.

For the next-generation experiments, it's the data quality rather than delensing methodologies which limits the efficiency of delensing, and the delensing ability of each different experiment is described by a delesing fraction factor $D$[53].

$$C_\ell^{delen} = Ant(\ell) D C_\ell^{lensing}. \tag{3.16}$$

If we only uses the internal delensing potential reconstruction of each experiment, called internal delensing or auto delensing, we will reach a relatively higher factor $D_{auto}$. The best possible delensing $D_{min}$ could be reached which is allowed by the instrumental constrains of the observed lensed CMB. $D_{auto}$ and $D_{min}$ are also listed in table below and we will relatively analyze the instruments later without delensing ($D = 1$), with internal delensing and with possible maximum delensing (with minimum coefficient $D = D_{min}$).

TABLE 3.1: Instrument abilities of removing the galactic foreground and abilities of internal delensing and maximum delesing .

| Instruments | $R_F$[52] | $D_{auto}$[53] | $D_{min}$[53] |
|---|---|---|---|
| LiteBIRD | 0.01 | 0.73 | 0.33 |
| CMB-S4 DW | 0.08 | 0.38 | 0.24 |
| CMB-S4 UD | 0.01 | 0.12 | 0.04 |
| SO LAT | 0.43 | - | - |
| SO SAT | 0.05 | 0.59 | 0.22 |
| PICO | 0.001 | 0.2 | 0.03 |

## 3.3 Systematic effects construction

### 3.3.1 Instrument configurations

#### White noise

The sensitivity $\sigma_n$ is depending on the operating frequency and polarization too. The sensitivity is at its minimum around 100GHz, and peaks at both low frequency and high frequency.

The total sensitivity is the statistical result over the full mission combining the different sensitivities at different frequency and the polarization sensitivity which will be lower than any sensitivity at a certain frequency. Except for Stage-4 we use the lowest sensitivity at 145GHz and regard it as the upper bound of the total sensitivity.

We will use these constant total values in the following investigations. Since this value is a constant, then it behaves like a white noise which has the same power in the power spectrum at every multipole.

To convert this constant $\sigma_n$ in unit of $\mu\text{K} \cdot \text{arcmin}$ to power spectrum,

$$C_\ell^{noise} = \left(\sigma_n \times \frac{1}{60}\frac{\pi}{180}\right)^2. \tag{3.17}$$

#### Sky coverage

The sky coverage of the space telescopes is not 100% as we discussed in 2.2.2. We simply takes the value as 80% avoiding the galactic plane where it's too noisy to have the signal from the CMB. For CMB-S4 deep and wide measurement the original sky coverage is around 70% and 60% is the result after avoiding the galactic plane. For other experiments, the sky coverage is completely depending on the strategies of the observation.

#### Frequencies

TABLE 3.2: Instrument working frequency bands

| Instruments | Frequency Band Central Frequencies (GHz) |
|---|---|
| LiteBIRD[24] | 40, 50, 60, 68, 78, 89, 100, 119, 140, 166, 195, 235, 280, 337, 402 |
| CMB-S4 | 10, 15, 20, 30, 40, 85, 95, 145, 155, 220, 270 |
| SO[26] | 27, 39, 93, 145, 225, 280 |
| PICO[27] | 21, 25, 30, 36, 43, 52, 62, 75, 90, 108, 129, 155, 186, 223, 268, 321, 385, 462, 555, 666, 799 |

We are going to study the foreground within several typical frequency bands. For LiteBIRD we will choose 100GHz, 140GHz and 195GHz; for CMB-S4 DW we will choose 95GHz, 145GHz, and 220GHz; for SO, we will choose 93GHz, 145 GHz and 225GHz; for PICO, we will choose 90 GHz, 155GHz, 223GHz.

### 3.3.2 Calibration errors

Following [21], polarization angle calibration mismatch, pointing direction calibration error and beam calibration imperfection were constructed as following.

**Polarization angle mismatch**

Theoretically we can achieve a analytical power-spectrum level solution by using the equation[54] describing the spherical harmonic coeficients:

$$\begin{aligned} E^{\circ}_{\ell,m} &= E_{\ell,m}\cos(2\alpha) - B_{\ell,m}\sin(2\alpha) \\ B^{\circ}_{\ell,m} &= E_{\ell,m}\sin(2\alpha) + B_{\ell,m}\cos(2\alpha) \end{aligned} \tag{3.18}$$

if there is a global polarization angle rotation $\alpha$ over the whole sky. If the primordial B-mode is 0 (or extremely weak compared to E-mode), with small polarization angle mismatch, typically $\alpha < 1^{\circ}$, the resulting B-mode keeps the Shape of E-mode and E-mode does not change:

$$\begin{aligned} E^{\circ}_{\ell,m} &\simeq E_{\ell,m} \\ B^{\circ}_{\ell,m} &\simeq E_{\ell,m}\cdot 2\alpha. \end{aligned} \tag{3.19}$$

We decided to do it at map-level, which should not make a big difference. We generated the CMB map in T,Q,U maps via *healpy.sphfunc.synfast* as told in 3.1.1 using the theoretical model with rigorously zero B-mode, $r = 0$. Only CMB map is considered here, because we want to see how the polarization angle mismatch can influence the result even if the foreground is removed.

At each pixel point on the map, T value remains the same and Q and U interchange with each other like a spin-2 spinor, as described in equation (A.5) then we performed a harmonic analysis on the new transformed map. Since the original B-mode signal is exactly 0, the B-mode signal of the new map denotes the residual signal of the B-mode that comes from the polarization angle mismatch.

**Random Pointing**

In the investigation of the influence from the random pointing, we can only do a map-level analysis. The map we used is still the generated CMB map itself in T,Q,U maps without any foreground.

We first got all the spherical coordinate of each pixels $(\theta, \phi)$ (with indices from 0 to $12N^2_{side} - 1$) on the T,Q,U maps. The coordinates and the indices of the pixels in the same location on the three maps are the same. $\theta$ is the polar angle and $\phi$ is the azimuth angle. We can use *healpy.pixfunc.pix2ang*.

Then to have the artificial random pointing, we re-mapped the T,Q,U maps simultaneously. We assigned a pair of pointing parameters $(\rho, \beta)$ where a radial parameter $\rho$ following a random absolute Gaussian distribution $|N(0, \sigma^2)|$ and a angular parameter $\beta$ following a random uniform distribution $U(0, 2\pi)$ to each point on the map. The choice of the coordinate system here is not important, as long as being a spherical coordinate system, since the angle $\beta$ assigned pointing does not care the specific choice. In default, it is galactic coordinates. The new coordinates of this point would be

$$(\theta, \phi) \Rightarrow (\theta + \rho\sin\beta, \phi + \frac{\rho\sin\beta}{\cos\theta}). \tag{3.20}$$

We should announce a regulation here to prevent the angular Fvalues exceeding the limit of the spherical coordinates: For new $\theta$, if $\theta < 0$, we do $\theta \to -\theta$; if $\theta > \pi$, then $\theta \to 2\pi - \theta$. For new $\phi$, if $\phi < 0$, we do $\phi \to 2\pi + \phi$; if $\phi > 2\pi$, we do $\phi \to \phi - 2\pi$.

This new position corresponds to a new pixel index, which could be obtained using *healpy.pixfunc.ang2pix*. Then using fancy indexing, a new map after the random pointing was generated. At last we performed a harmonic analysis on the new map.

The resulting non-zero B-mode is the spurious signal from the random pointing, because the original B-mode signal is exactly 0 also.

**Beam calibration imperfection**

First let's begin with the LiteBIRD. The central beam is set to be a Gaussian with FWHM 30′.

The sidelobes with responses below -39 dB and above -50 dB is measured in the laboratory[55]. LiteBIRD central beam's response reduces to -39 dB at 0.9° and the sidelobes' response reduce to -50 dB at 20 degree away from the pointing direction. Beyond -50 dB, or farther than 20 degrees the response is unknown. We followed [21] and proposed one beam which remains the trend of the measured beam, and another auxiliary beam is smaller than the previous one with a factor of $\left(\frac{\theta_0}{\theta}\right)^{20}$, where $\theta_0$ is the truncation angle, i.e., here is 20 degrees. With the power of 20, the second beam diminishes very quickly when $\theta$ increases. The spurious signal is generated from the difference between these two beams. The extended beam and the auxillary beam form a largest mis-calibration since the extended beam can be regared as the strongest possible sidelobe and the auxiliary one can be regared as the weakest possible sidelobe, because the sidelobes have the trend to diminish when away from the central beam, and they can not diminish like a sharp step since there is diffraction etc. So the spurious signal produced by these two beams can be considered as an upper bound of the amount of the beam mis-calibration.

For simplicity, we can write the first whole beam profile as ″20 degree Far-sidelobe″ or ″20 deg FSL″; and the second whole beam profile with the truncated auxiliary beam at 20 degree as ″cutted 20 degree Far-sidelobe″ or ″ cutted 20 deg FSL″. They are shown in solid and dashed blue curves respectively in the figure below.

Although the LiteBIRD's sidelobes are fixed above -50 dB, to see whether sidelobes with smaller truncation angle $\theta_0$, i.e., sidelobes attenuate more quickly and reach -50 dB nearer to the central beam, would potentially affect the LiteBIRD results and in the same time we need to explore the different sidelobe-effect in other experiments, we followed [21], constructed a beam profile with $\theta_0 = 10°$ and another auxiliary beam with the same factor $\left(\frac{\theta_0}{\theta}\right)^{20}$. These two beams are written as ″10 degree Far-sidelobe″ or ″10 deg FSL″ and ″cutted 10 degree Far-sidelobe″ or ″ cutted 10 deg FSL″ are shown below in solid and dashed orange curves respectively.

″15 degree Far-sidelobe″ or ″15 deg FSL″ is the average between ″10 deg FSL″ and ″20 deg FSL″. Then ″cutted 15 degree Far-sidelobe″ or ″ cutted 15 deg FSL″ applies the same rule as before. They are shown in figure 3.4 in green solid and dashed curves respectively. Notice all of the six beam above share the same central beam.

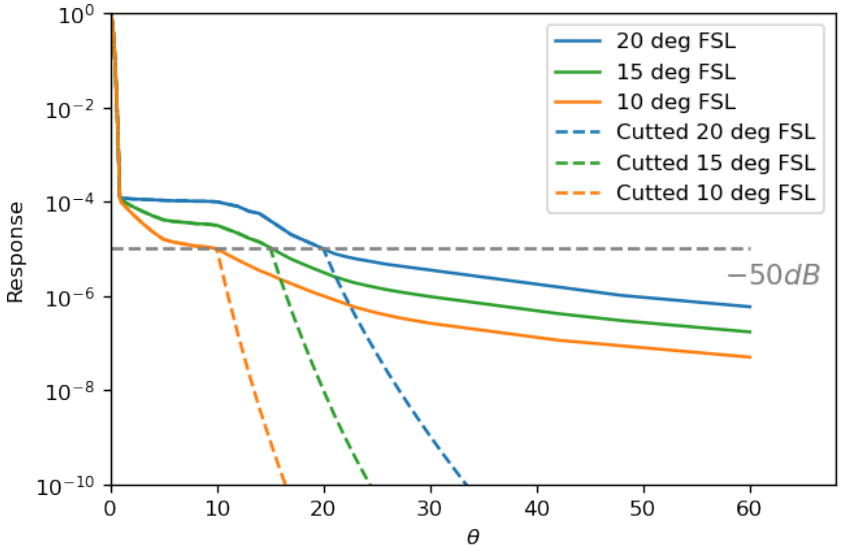


FIGURE 3.4: Beam profiles and their auxiliary beams with the same 30′ central beam but different far-sidelobes reach -50dB at 10°, 15°, and 20°.

After the transformation, The resulting window functions in multipoles $b(\ell)$ should be normalized and to do this we set the $b(\ell = 0) = 1$ and all $b(\ell)$ are divided by the original $b(\ell = 0)$. Three beam window functions and their auxiliary beams are shown in figure 3.5.

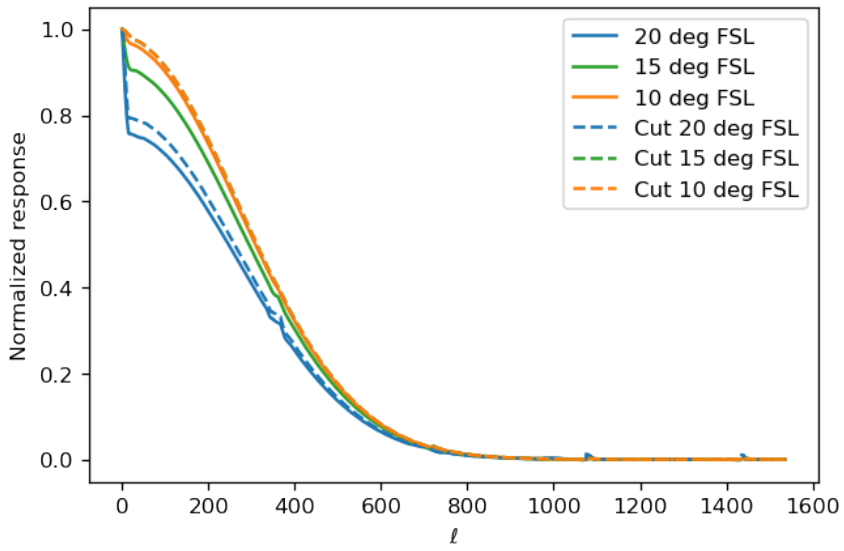


FIGURE 3.5: Normalized beam window functions and their auxiliary beams in multipole $\ell$ with the same 30′ central beam and far-sidelobes reach -50dB at 10°, 15° and 20°.

We extrapolate the LiteBIRD's three far-sidelobe constructions to the rest of the six instruments since we don't have the beam calibration results for the rest instruments yet. The only beam difference between the instruments is the scale. In other words, we reasonably believed that the widths of the central Gaussian beam and far-sidelobes change proportionally between instruments because the sidelobes are the influences of the telescope baffle whose size is related with the aperture, on which

the central beam with is depending. For example the Large Aperture Telescope with central beam FWHM 1.4′, has the beam looks like figure 3.6.

The sidelobes no longer have the truncation angle 20, 15, 10 degrees, so we just all them A, B, and C in a decreasing sequence of the truncation angle.

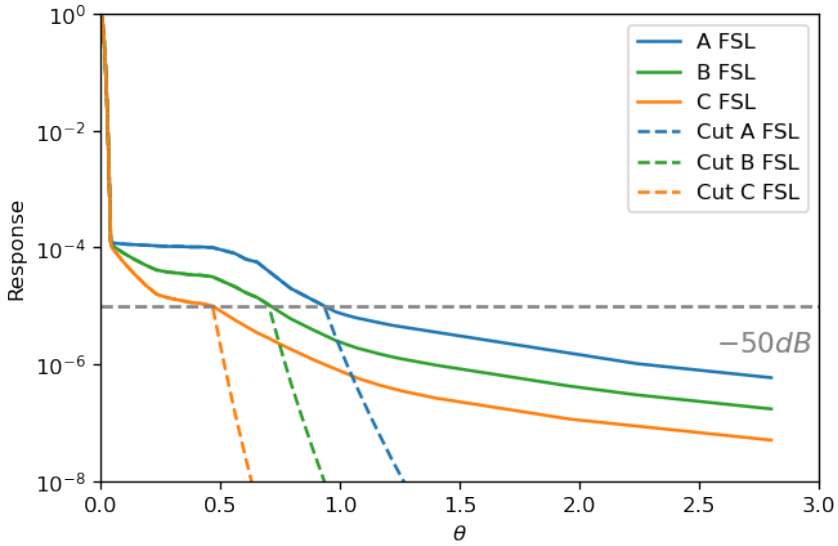


FIGURE 3.6: Beam profiles and their auxiliary beams with the same 1.4′ central beam but different far-sidelobes reach -50dB at 0.93°, 0.70°, and 0.47°, named A,B,C.

However the beam window function in multipoles in figure 3.7 is quite different from LiteBIRD.

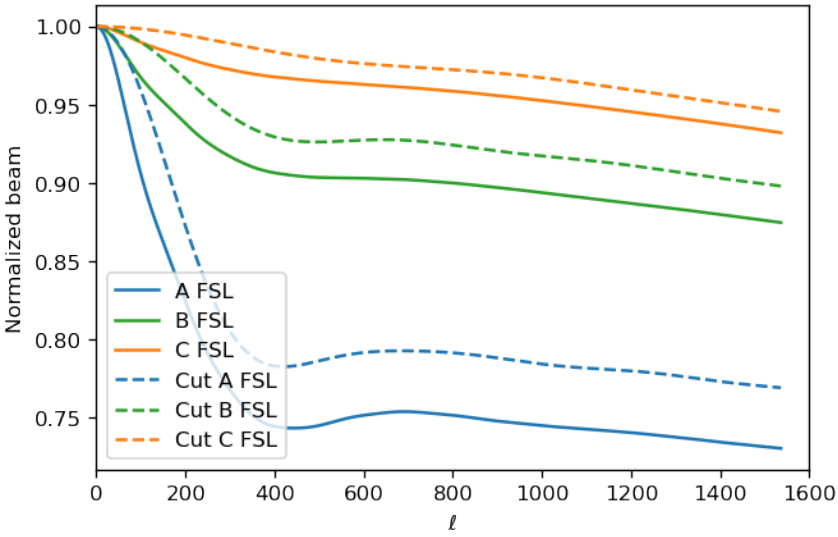


FIGURE 3.7: Normalized beam window functions and their auxiliary beams in multipole $\ell$ with the same 1.4′ central beam and far-sidelobes A, B, and C.

Later, all the far-sidelobes are named A, B, C.

The noises of the beam calibration imperfection are mainly comes from the convolution between the wrong far-sidelobes and the strong foreground. Therefore we

only considered the foreground map containing dust and synchrotron emissions, generated from PySM as described in 3.1.3.

Here comes the importance of the frequency bands. At different frequency the foreground signal appears differently. We generated the foreground maps in three different frequencies for each experiment, and the frequencies are shown in 3.3.1.

After we convoluted two beam profiles with the foreground map, we made the difference between these two convoluted map which denotes the residual signal that comes from the beam differences. Then we performed harmonic analysis onto the residual map with the corresponding mask for each experiment shown in section 3.1.5, the B-mode residuals could be obtained.

## 3.4 Systematics influence on the error of $r$

If we consider only the noise, foreground after the component separation, and the weak lensing with internal delensing ($D_{auto}$) but no other systematic effects, the upper bound of the error in $r$ will be

$$\sigma_r^{base} \simeq \frac{0.1}{\sqrt{f_{\rm sky}}} \left\{ \sum_{\ell=\ell_{\rm min}}^{\ell_{\rm max}} \frac{(2\ell+1)}{2} \left[ \frac{Ant(\ell) C_\ell^{\rm PGWB}(r=0.1)}{C_\ell^{noise} + C_\ell^{fore} + C_\ell^{delen}} \right]^2 \right\}^{-1/2}, \tag{3.21}$$

and because of its delensing generality it is considered as the baseline of the error, which is going to be compared with those caused by systematic effects, denoted by the index $j$,

$$\sigma_r^{'} \simeq \frac{0.1}{\sqrt{f_{\rm sky}}} \left\{ \sum_{\ell=\ell_{\rm min}}^{\ell_{\rm max}} \frac{(2\ell+1)}{2} \left[ \frac{Ant(\ell) C_\ell^{\rm PGWB}(r=0.1)}{C_\ell^{noise} + C_\ell^{fore} + C_\ell^{delen} + \sum_j C_\ell^{\rm j}} \right]^2 \right\}^{-1/2}. \tag{3.22}$$

The beam convolution effect of the spectra should be taken into account, so the PGWB spectrum is multiplied by $Ant(\ell)$ and other spectra $C_\ell^{noise}$, $C_\ell^{fore}$, $C_\ell^{delen}$ are well defined in previous sections.

We are going to figure out how much do the systematic effects increase the level of the original uncertainty of $r$ caused by external effect and noise, defined by a increment factor $\eta$:

$$\boxed{\eta = \frac{\sigma_r^{'}}{\sigma_r^{base}} - 1.} \tag{3.23}$$

We would like to figure out how much the systematic effects are that will cause a 1% increasing in the error in $r$. These critical value of the systematic effects can serve as a guideline in the future calibrations.

# Chapter 4

# Results

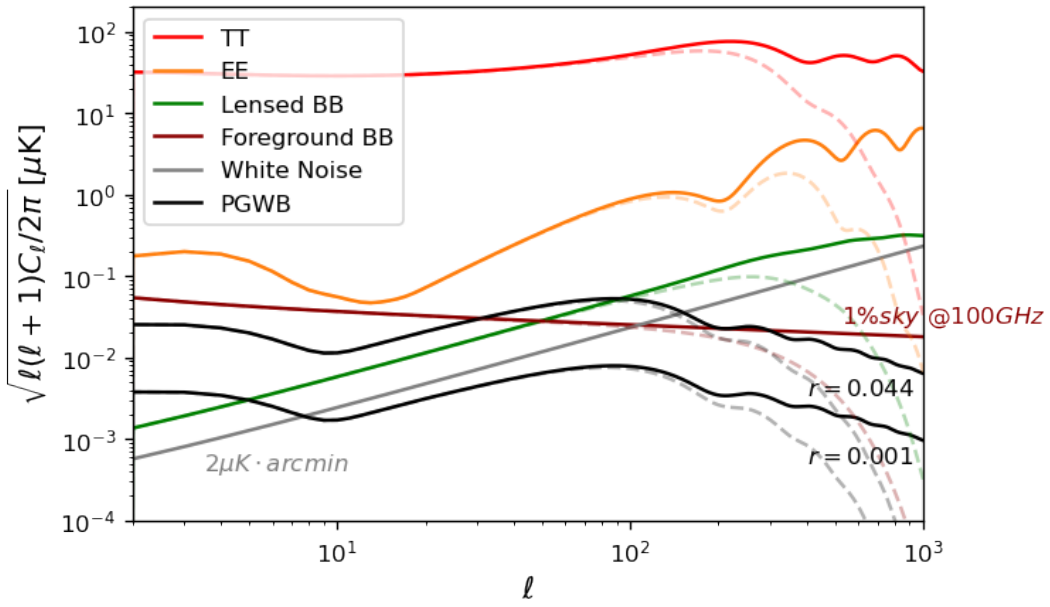


FIGURE 4.1: An illustration of the foreground B-mode signal $C_\ell^{clean}$ at 100GHz in the 1% cleanest sky region, together with a lensed B-mode signal comes from the weak lensing $C_\ell^{lensing}$ and a white noise with a typical sensitivity 2 $\mu K\cdot'$ comparing to the temperature power spectrum, E-mode power spectrum and the primordial B-mode spectrum with the tensor-to-scalar ratio level $r = 0.001$, which is targeted by the next-generation experiments and its latest upper bound $r = 0.044$, which is constrained now by Planck and BICEP2/Keck 2015 data[7]. Dashed lines are the power spectra convoluted with a 30′ FWHM beam except the white noise.

## 4.1 Pure foreground effect

While $f_{sky} = 100\%$, and if there is no component separation and delensing applied, the upper bound of the error in $r$ caused by only the foreground, including the galactic foregrounds and the weak lensing is

$$\sigma_r^{fore} = 0.000571 \tag{4.1}$$

to the sixth decimal places.

A lower upper bound in the error of $r$ can be reached if we can apply component separation and delensing protocol as we said in section 3.2.1 and 3.2.2 for each experiment [53].

## 4.2 Different sensitivities, component separation abilities and delensing capabilities

For each experiment, counting for its sky coverage and sensitivity, the upper bound of the error in $r$ is showed in the table below.

TABLE 4.1: Upper bound of the error in $r$ caused by the external effects, sensitivity, and sky coverage for each experiment, and then constrained by their component separation and delensing abilities.

(A) No component separation nor delesing.

| Instruments | $\sigma_r^{no}$ |
|---|---|
| LiteBIRD | 0.000832 |
| S-4 DW | 0.000905 |
| S-4 UD | 0.003386 |
| SO LAT | 0.001812 |
| SO SAT | 0.002024 |
| PICO | 0.000745 |

(B) With component separation but no delesing.

| Instruments | $\sigma_r^{cs}$ |
|---|---|
| LiteBIRD | 0.000421 |
| S-4 DW | 0.000593 |
| S-4 UD | 0.001684 |
| SO LAT | 0.001567 |
| SO SAT | 0.001235 |
| PICO | 0.000172 |

(C) With component separation and internal delesing ($D_{auto}$), acting as the baseline.

| Instruments | $\sigma_r^{base}$ |
|---|---|
| LiteBIRD | **0.000340** |
| S-4 DW | **0.000341** |
| S-4 UD | **0.000318** |
| SO LAT | **0.001567** |
| SO SAT | **0.000838** |
| PICO | **0.000066** |

(D) With component separation and maximum delesing ($D_{min}$).

| Instruments | $\sigma_r^{min}$ |
|---|---|
| LiteBIRD | 0.000207 |
| S-4 DW | 0.000282 |
| S-4 UD | 0.000171 |
| SO LAT | 0.001567 |
| SO SAT | 0.000467 |
| PICO | 0.000019 |

The errors in third table (C) with bold font will be regarded as the comparison baselines, since we can do delensing but maybe not to the optimum. Since the Large Aperture Telescope of the Simons Observatory do not have delensing profile and it is not aimed for direct detecting of the B-mode, we will pay less attention onto it. We can see among all the experiments, clearly PICO has an extraordinary capability to detect $r$.

Now we are going to have the results of the influence from the systematics or calibrations for all the instruments.

## 4.3 Polarization angle mismatch

### 4.3.1 LiteBIRD

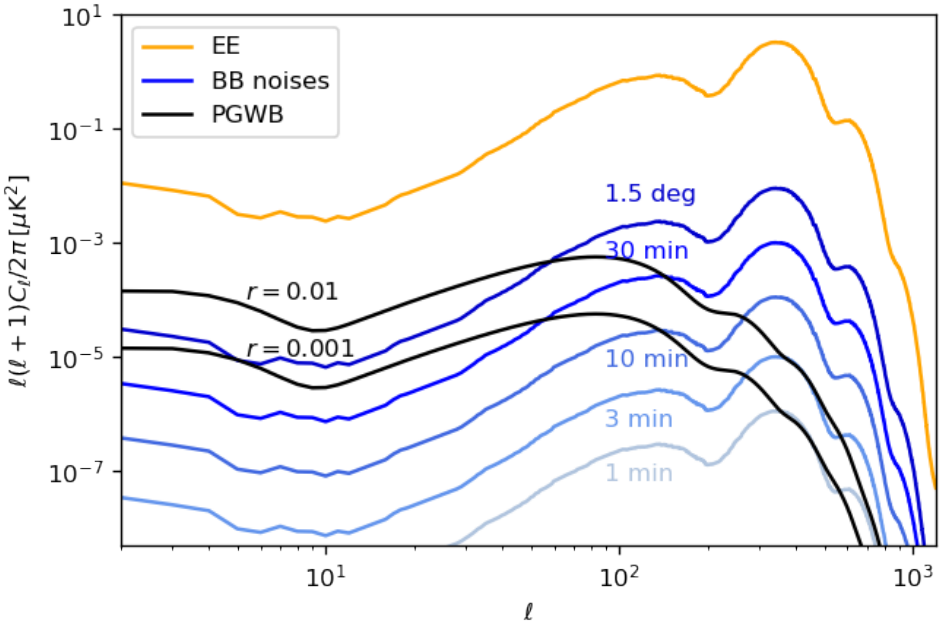


FIGURE 4.2: An illustration of B-mode Noises caused by different polarization angle mismatches with LiteBIRD's 30′ central beam FWHM

We can see that the B-mode signal generated by this polarization angle mismatch preserve the shape of the original E-mode signal in the power spectrum, and the amplitude of this spurious signal is depending on the mismatch angle.

Then we calculated the error in $r$ using different mismatch angles, compared with the previous baselines of the error in $r$. We listed the results in the table below and found the error value increases monotonically when the global mismatched polar angle increases:

TABLE 4.2: The increased ratio of the upper bound of the error in $r$ caused by different global mismatched polarization angle for LiteBIRD

| Mismatched polarization angle $\alpha$ | $\eta$ |
|---|---|
| 1′ | 0.0085% |
| 3′ | 0.0764% |
| 10′ | 0.8383% |
| 12′ | 1.1999% |
| 14′ | 1.6218% |
| 16′ | 2.1019% |
| 18′ | 2.6377% |
| 20′ | 3.2267% |
| 24′ | 4.5552% |
| 30′ | 6.8908% |
| 90′ | 46.3254% |

We can see 1% increasing of the error ($\delta_{\sigma_r} = 3 \times 10^{-6}$) corresponds to a global polarization angle mismatch around 11′ for LiteBIRD.

**Comparison with the polar angle requirement from the view of biases in $r$**

For the most restrictive case that all the detectors and frequency bands are correlated, the strongest requirement of the polarization angle uncertainties should be less than 1′ in order not to induce biases on $r$ larger than 1% ($\delta_r = 5.77 \times 10^{-6}$) of the total budget of the systematics to the overall sensitivity [29]. We can draw a conclusion here that to restrict the increasing of the bias of $r$ requires much more precision in the polarization angle calibration than to restrict the increasing of the uncertainty of $r$, at least for LiteBIRD.

### 4.3.2 Stage-4

TABLE 4.3: The increased ratio of the upper bound of the error in $r$ caused by different global mismatched polarization angle for Stage-4 measurements

(A) Deep and wide measurement

| Mismatched polarization angle $\alpha$ | $\eta$ |
|---|---|
| 1′ | 0.0070% |
| 3′ | 0.0633% |
| 10′ | 0.7017% |
| 12′ | 1.0094% |
| 14′ | 1.3725% |
| 16′ | 1.7904% |
| 18′ | 2.2627% |
| 20′ | 2.7891% |
| 24′ | 4.0020% |
| 30′ | 6.2122% |
| 90′ | 50.1091% |

(B) Ultra-deep measurement

| Mismatched polarization angle $\alpha$ | $\eta$ |
|---|---|
| 1′ | 0.0325% |
| 3′ | 0.2921% |
| 5′ | 0.8098% |
| 7′ | 1.5832% |
| 10′ | 3.2134% |
| 12′ | 4.6060% |
| 14′ | 6.2360% |
| 16′ | 8.0962% |
| 18′ | 10.1792% |
| 20′ | 12.4769% |
| 30′ | 26.9040% |

For deep and wide measurement of the Stage-4, 1% increasing of the error corresponds to around 12′ global polarization angle mismatch, similar to LiteBIRD; in contrast, ultra-deep measurement requires a global polarization angle mismatch less than 7′ to get 1% of error increasing, nearly half of the previous one.

### 4.3.3 The Simons Observatory

For the Large Aperture Telescope of the Simons Observatory, the requirements on the polarization angle calibration will not be strict. Thanks to its high noise level, the baseline of the error in $r$ has already been quite large. the increasing of the error due to polarization angle is negligible. Even a 22′ angle mismatch will cause less than 1% of the error in $r$.

However, for the Small Aperture Telescope, to reach a error increasing level less than 1% we need to calibrate its polarization angle accuracy within 13′, similar to LiteBIRD.

TABLE 4.4: The increased ratio of the upper bound of the error in $r$ caused by different global mismatched polarization angle for the Simons Observatory measurements

(A) Large Aperture Telescope

| Mismatched polarization angle $\alpha$ | $\eta$ |
|---|---|
| 1′ | 0.0020% |
| 3′ | 0.0179% |
| 10′ | 0.1987% |
| 14′ | 0.3891% |
| 18′ | 0.6428% |
| 20′ | 0.7932% |
| 22′ | 0.9594% |
| 24′ | 1.1411% |
| 26′ | 1.3384% |
| 28′ | 1.5513% |
| 30′ | 1.7797% |
| 90′ | 15.4244% |

(B) Small Aperture Telescope

| Mismatched polarization angle $\alpha$ | $\eta$ |
|---|---|
| 1′ | 0.0066% |
| 3′ | 0.0596% |
| 5′ | 0.1654% |
| 10′ | 0.6605% |
| 12′ | 0.9503% |
| 14′ | 1.2921% |
| 16′ | 1.6857% |
| 18′ | 2.1306% |
| 20′ | 2.6265% |
| 24′ | 3.7694% |
| 30′ | 5.8540% |
| 90′ | 47.4277% |

### 4.3.4 PICO

TABLE 4.5: The increased ratio of the upper bound of the error in $r$ caused by different global mismatched polarization angle for PICO

| Mismatched polarization angle $\alpha$ | $\eta$ |
|---|---|
| 1′ | 0.0796% |
| 3′ | 0.7083% |
| 5′ | 1.9281% |
| 7′ | 3.6722% |
| 10′ | 7.0895% |
| 12′ | 9.7805% |
| 14′ | 12.7178% |
| 16′ | 15.8458% |
| 18′ | 19.1234% |
| 20′ | 22.5223% |
| 30′ | 40.9024% |

Because PICO's baseline of the error in $r$ is extremely small, we can see 1% increasing of the error corresponds to a global polarization angle mismatch less than 5′ for PICO, which is a very strict constrain.

## 4.4 Random pointing

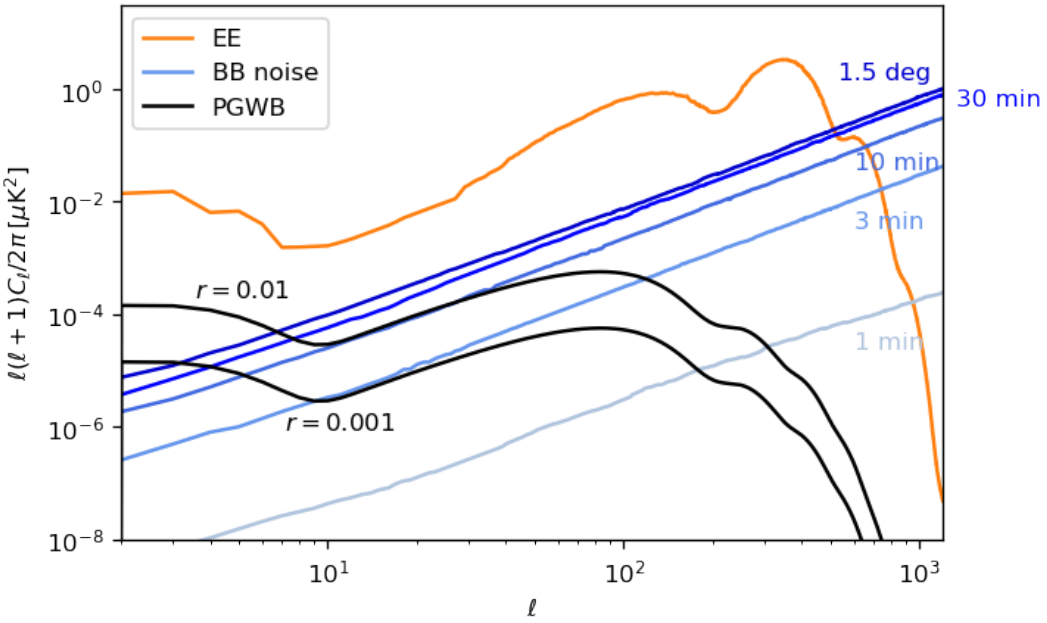


FIGURE 4.3: An illustration of the B-mode Noises caused by random pointing error with different radial pointing uncertainties $\sigma$ with 30′ central beam FWHM, typically for LiteBIRD. Unlike the situation in polarization angle mismatch, here when the random pointing uncertainties increases, there will be a plateau of the noise, because the map remapping is too random and lost all the information, as we can see that 1.5 degree uncertainty does not increase the noise much from 30′ uncertainty. This phenomenon is very clear in PICO. See below 4.4.3

TABLE 4.6: The increased ratio of the upper bound of the error in $r$ caused by different levels of the random pointing for LiteBIRD

| Pointing error FWHM | $\eta$ |
|---|---|
| 1′ | 0.1370% |
| 1.5′ | 0.1042% |
| 2′ | 0.1144% |
| 2.5′ | 0.1433% |
| 3′ | 0.3431% |
| 3.5′ | 0.7702% |
| 4′ | 1.4088% |
| 5′ | 3.7407% |
| 6′ | 6.3659% |
| 7′ | 9.4622% |
| 8′ | 12.7971% |
| 9′ | 15.4917% |
| 10′ | 18.6265% |
| 15′ | 33.9180% |
| 20′ | 51.4014% |

Due to the low resolution of the analysis $N_{side} = 512$, we can see the noise level is quite unstable below 2′ pointing error, but they are very weak at the same time. There's no problem to just ignore them.

We can see 1% increasing of the error corresponds to a 3.5′ to 4′ FWHM of pointing direction error about 1/8 of the beam FWHM. Within 1.5 degrees, the error in $r$ monotonically increases while the pointing error increases.

### 4.4.1 Stage-4

Both deep and wide measurement and ultra-deep measurement of Stage-4 have excellent angular resolutions around 1.5′ at 145GHz. It's reasonable to expect the precision and the accuracy of the positioning to be better than the beam resolution otherwise the observation losses its meaning, and a calibration based on celestial object with good resolution can lead to an precise pointing also. Thus we thought the random pointing error angle would be smaller than the angular resolution, i.e., smaller than 1′ which causes an ignorable noise. Besides, our resolution $N_{side} = 512$ does not allow us to do any finer analysis.

### 4.4.2 The Simons Observatory

The same reason above can be applied to the Large Aperture Telescope of the Simons Observatory with a 1.4′ resolution FWHM. For only the Small Aperture Telescope, we have the following results.

TABLE 4.7: The increased ratio of the upper bound of the error in $r$ caused by different levels of the random pointing for the Small Aperture Telescope of the Simons Observatory

| Pointing error FWHM | $\eta$ |
|---|---|
| 1′ | 0.2722% |
| 1.25′ | 0.2530% |
| 1.5′ | 0.2411% |
| 1.75′ | 0.1862% |
| 2′ | 0.2647% |
| 2.25′ | 0.3387% |
| 2.5′ | 0.6762% |
| 2.75′ | 1.2090% |
| 3′ | 2.1145% |
| 3.5′ | 5.2573% |
| 4′ | 11.2427% |
| 5′ | 28.1573% |
| 6′ | 47.9778% |
| 7′ | 74.3230% |
| 8′ | 97.0448% |
| 9′ | 119.2969% |
| 10′ | 136.6867% |
| 15′ | 240.3124% |
| 20′ | 332.5193% |

We can see 1% increasing of the error corresponds to a FWHM of pointing direction error slightly smaller than 2.75′, about 1/7 of the beam FWHM. We find this

configuration's error in $r$ increase much faster than that in LiteBIRD when the pointing error increases. At a 17′ level of the pointing error, equivalent to the beam size, we would expect there is a 300% of the error increasing.

### 4.4.3 PICO

TABLE 4.8: The increased ratio of the upper bound of the error in $r$ caused by different levels of the random pointing for PICO

| Pointing error FWHM | $\eta$ |
|---|---|
| 1′ | 1.7229% |
| 1.25′ | 1.3166% |
| 1.5′ | 1.6804% |
| 1.75′ | 1.8458% |
| 2′ | 2.3575% |
| 2.25′ | 5.2986% |
| 2.5′ | 10.1386% |
| 2.75′ | 23.1146% |
| 3′ | 34.6469% |
| 3.5′ | 93.2451% |
| 4′ | 156.9431% |
| 5′ | 421.9935% |
| 6′ | 377.3304% |
| 7′ | 673.1471% |
| 8′ | 797.2133% |
| 9′ | 2085.4261% |
| 10′ | 1528.0941% |
| 15′ | 2618.3918% |
| 20′ | 2189.8399% |

Only by looking the results, because of the computation limit, it is hard to tell at which level of the FWHM of pointing direction error in PICO can cause exactly 1% increasing of the error in $r$, but we can sure this value could not go beyond 1.5′. Probably it is less than 1′ and is about 1/7 of the central beam FWHM.

We found this configuration's error in $r$ increase dramatically when polarization error increases. Even just with a 6.2′ level of the pointing error, equivalent to the beam size, the ability of this best configuration that lowers the error in $r$ among these 6 experiments will be devastated.

Besides, we see the noise plateau, which remains around 20 times increment of the error in $r$ when FWHM of pointing direction error goes beyond 9′. This is because the remapping is too random and exceeding the telescope's resolution, they mixed the pixels and lost all the original information. No matter what the FWHM of the random pointing is, as long as it is large enough, the remapped maps are similar to each other.

In addition, if the resolution of the telescope is low enough, the beam helps the random pointing to camouflage under the blurred map. However, unlike LiteBIRD, PICO has a good resolution, and thus the effect of the random pointing has no where to hide.

## 4.5 Beam calibration imperfection

### 4.5.1 LiteBIRD

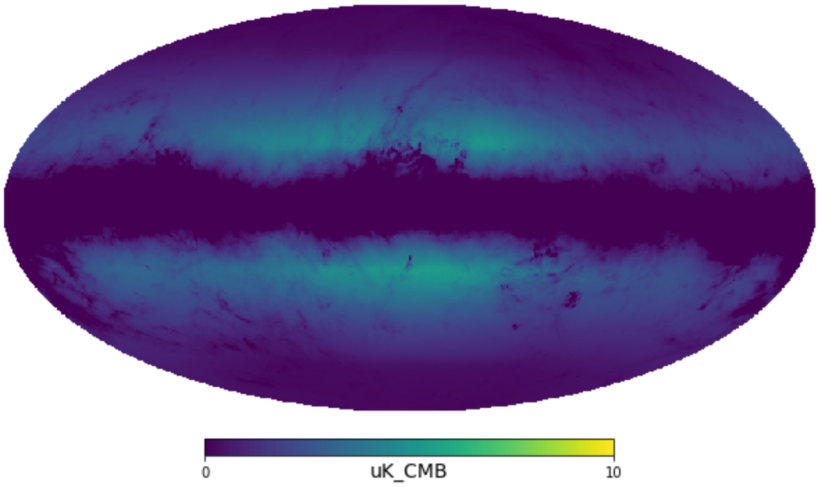


FIGURE 4.4: An illustration of the residual signal in 100GHz temperature map caused by beam calibration imperfection of LiteBIRD (calibration error occurs between its '20 deg FSL' and 'cut 20 deg FSL'). This wrongly calibrated far-sidelobe pick up the strong signal from the galactic disk and therefore the positive spurious signal spreads on the both sides of the galactic plane.

#### 100GHz

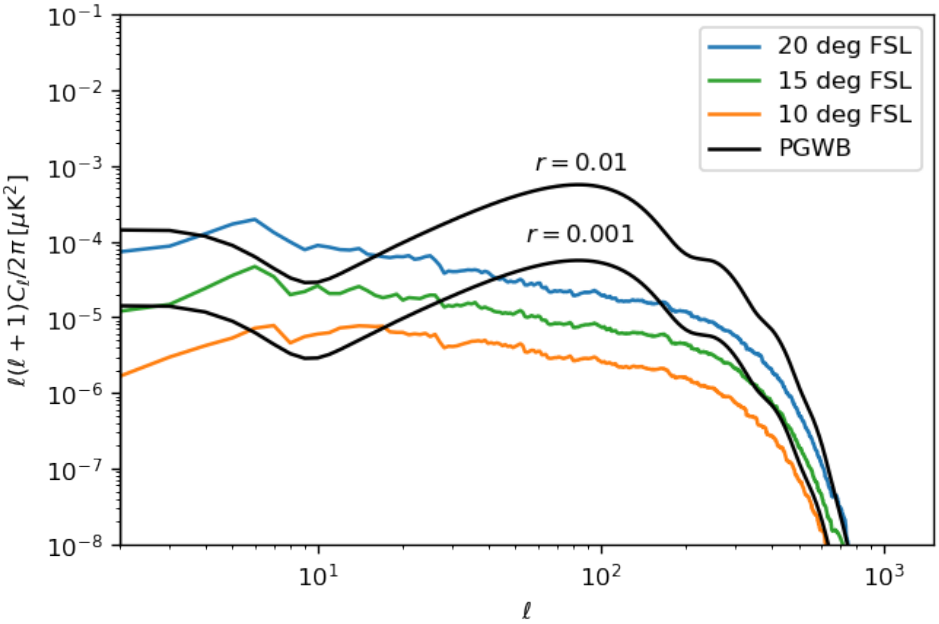


FIGURE 4.5: An illustration of the B-mode residual signals caused by three kinds of beam calibration imperfection at 100GHz

**140GHz**

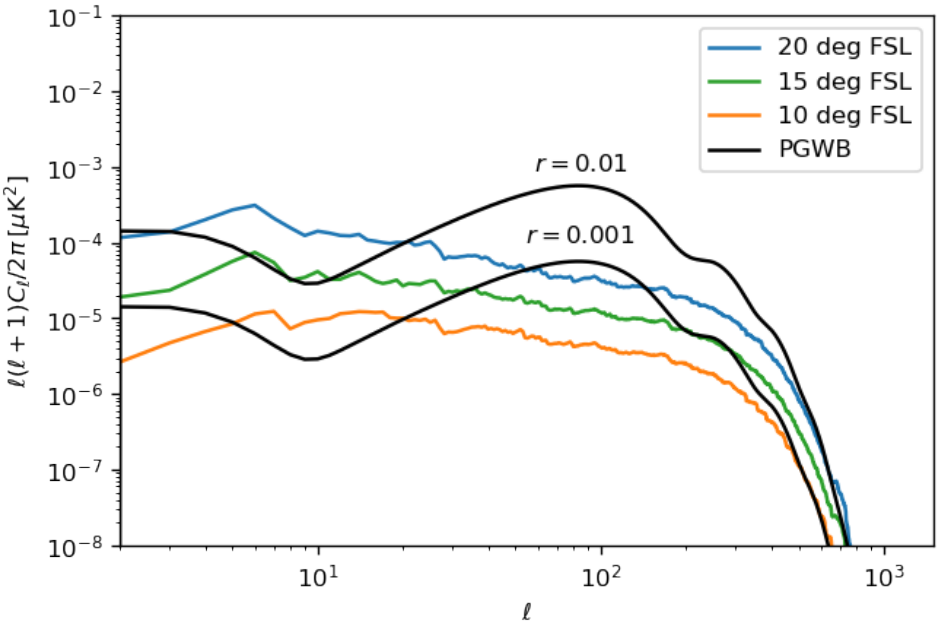


FIGURE 4.6: An illustration of the B-mode residual signals caused by three kinds of beam calibration imperfection at 145GHz, higher than the residuals at 100GHz.

**195GHz**

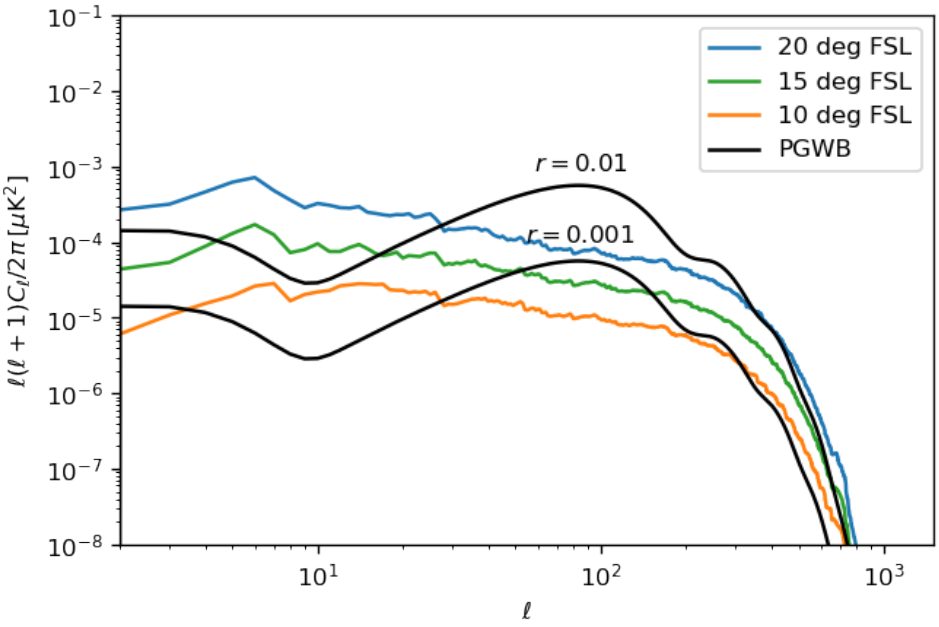


FIGURE 4.7: An illustration of the B-mode residual signals caused by three kinds of beam calibration imperfection at 195GHz, even higher than those at 145GHz.

**Average**

After getting all the results, we will take an average between 3 different frequency bands to show an overall error increasing affected by the beams. Higher frequency (within 100-195GHz), stronger the residual, it's obvious and trivial because galactic foreground is indeed stronger at larger frequencies (within 100-195GHz).

Results and the average values for LiteBIRD are shown below.

TABLE 4.9: The increased ratio of the upper bound of the error in $r$ caused by different mis-calibrated far-sidelobes in three typical frequency bands and their averages for LiteBIRD.

| Truncation angle $\theta_0$ | $\eta$ @100GHz | $\eta$ @145GHz | $\eta$ @195GHz | Average |
|---|---|---|---|---|
| 20° | 19.7687% | 24.2306% | 35.8743% | 26.6245% |
| 15° | 10.6972% | 13.8242% | 21.1459% | 15.2224% |
| 10° | 3.6579% | 5.3862% | 10.0849% | 6.3797% |

We found in reality, LiteBIRD would have its maximum error increasing in $r$ around 27% since its beam has been fixed within 20 degrees[55] and the auxiliary beam 'cutted 20 deg FSL' has almost the largest difference between the extended beam after 20 degrees as we have said before. Thus these two beams cause the largest error. We also explore the possibility that LiteBIRD with other two kinds of similar beams, truncated at 10 degrees and 15 degrees. The error is increasing while the truncated angle value increases.

### 4.5.2 Stage-4

TABLE 4.10: The increased ratio of the upper bound of the error in $r$ caused by different mis-calibrated far-sidelobes in three typical frequency bands and their averages for Stage-4 measurements.

(A) Deep and wide measurement

| Far-sidelobe | $\eta$ @95GHz | $\eta$ @145GHz | $\eta$ @220GHz | Average |
|---|---|---|---|---|
| A | 1.6533% | 2.9387% | 9.8016% | 4.7979% |
| B | 0.2724% | 0.4848% | 1.6293% | 0.7955% |
| C | 0.0428% | 0.0762% | 0.2566% | 0.1252% |

(B) Ultra-deep measurement

| Far-sidelobe | $\eta$ @95GHz | $\eta$ @145GHz | $\eta$ @220GHz | Average |
|---|---|---|---|---|
| A | 84.4990% | 144.1925% | 411.2439% | 203.3118% |
| B | 14.9318% | 26.1906% | 83.6774% | 41.5989% |
| C | 2.0231% | 3.5926% | 11.9341% | 5.8499% |

For DW measurement of CMB-S4, situation is in the concordance with LiteBIRD: error increases while the truncation angle increases. Beam difference with C FSL generate the smallest error, only 0.1%.

However for UD measurement of CMB-S4, which has a similar baseline as DW's but it observes only an extremely small sky region, things become pessimistic if there is an A FSL.

### 4.5.3 the Simons Observatory

TABLE 4.11: The increased ratio of the upper bound of the error in $r$ caused by different mis-calibrated far-sidelobes in three typical frequency bands and their averages for the Simons Observatory.

(A) Large Aperture Telescope

| Far-sidelobe | $\eta$ @93GHz | $\eta$ @145GHz | $\eta$ @225GHz | Average |
|---|---|---|---|---|
| A | 0.6739% | 1.2217% | 4.4959% | 2.1305% |
| B | 0.1115% | 0.2022% | 0.7468% | 0.3535% |
| C | 0.0150% | 0.0272% | 0.1005% | 0.0476% |

(B) Small Aperture Telescope

| Far-sidelobe | $\eta$ @93GHz | $\eta$ @145GHz | $\eta$ @225GHz | Average |
|---|---|---|---|---|
| A | 27.6187% | 42.8519% | 112.0634% | 60.8447% |
| B | 12.8598% | 20.3995% | 53.7546% | 87.0139% |
| C | 5.6457% | 9.3030% | 25.1770% | 13.3752% |

For Large Aperture Telescope of the Simons Observatory, situation is similar to deep and wide measurement of Stage-4 (actually all their beams are the same): error increases when truncation angle increases, but with much smaller increasing ratio $\eta$ because it has higher baselines. From these small values we can draw a conclusion that beam calibration error does not affect LAT a lot.

On the other hand, for Small Aperture Telescope of the Simons Observatory, the increments are quite large because of its smaller sky coverage and lower baseline than LAT.

### 4.5.4 PICO

TABLE 4.12: The increased ratio of the upper bound of the error in $r$ caused by different mis-calibrated far-sidelobes in three typical frequency bands and their averages for PICO.

| Far-sidelobe | $\eta$ @90GHz | $\eta$ @155GHz | $\eta$ @223GHz | Average |
|---|---|---|---|---|
| A | 42.7519% | 69.5658% | 134.8038% | 74.7072% |
| B | 12.5455% | 24.0086% | 57.3245% | 31.2929% |
| C | 2.4053% | 5.0441% | 14.5099% | 7.3198% |

PICO also has the same property that the error increases when truncation angle increases, but the situation is more severe than LiteBIRD because of its low baseline of the error in $r$. For beams with C FSL, the increment of error in $r$ is similar to the LiteBIRD (corresponding to LiteBIRD 10 degree FSL). However, For beams with A FSL or B FSL, the situation is more severe than LiteBIRD (corresponding to 20 and 15 degree FSL).

## 4.6 Combination of the systematic effects

According to the definition of the error in $r$, the systematics are not linear and thus their effects in the error in $r$ are not addible. So it is necessary to re-evaluate the effects when combine them together. We are going to select some representative configuration for each experiment.

We will choose the polarization mismatch angle and random pointing FWHM which correspond or close to have the 1% increment $\eta = 1\%$ for all the experiments. As for the beam calibration imperfection, we would choose the medium frequency band of the three bands for each experiment, and the far-sidelobe type which is close to have $\eta = 1\%$ and plus a 20 degree far-sidelobe case for LiteBIRD (since it is the real case).

TABLE 4.13: Combinational effect on the instruments. The increments $\eta$ caused by single effect are also listed in the parentheses. Note that the increment after the combination must be greater than those of the sigle effect for a certain experiment.

| Instruments | Mismatched polarization angle $\alpha$ | Pointing error FWHM | Far-sidelobe | Overall $\eta$ |
|---|---|---|---|---|
| LiteBIRD (real) | 10′ (0.8383%) | 3.5′ (0.7702%) | 20° (24.2306%) | 25.9117% |
| LiteBIRD | 10′ (0.8383%) | 3.5′ (0.7702%) | 10° (5.3862%) | 6.9460% |
| S-4 DW | 12′ (1.0094%) | - | B (0.4848%) | 1.4926% |
| S-4 UD | 5′ (0.8098%) | - | C (3.5926% ) | 4.3994% |
| SO LAT | 22′ (0.9594%) | - | A (1.2217%) | 2.1779% |
| SO SAT | 12′ (0.9503%) | 2.75′ (1.2090%) | C (9.3030%) | 11.6377% |
| PICO | 3′ (0.7083%) | 1.25′ (1.3166%) | C (5.0441% ) | 7.0754% |

The results show a quite good linearity that we did not predict.

For LiteBIRD, especially in the real case, the beam calibration error should be responsible for almost all the $r$ error increament. The best we can do is to reduce the polarization angle mismatch and pointing error but it will not assist so much. For a similar configuration but with a smaller uncalibrated far-sidelobe, the situation will be better and then we can start to consider the other two calibrations.

We could say, DW measurement of CMB-S4 together with LAT of Simons observatory have the most lenient calibration requirement for these three types of systematics among all the experiments. PICO's calibration requirement is the most strict one, every kind of systematics should be calibrated carefully in order not to ruin its excellent performance. PICO is then followed by UD measurement of CMB-S4. For SAT of Simons observatory, the calibration of the pointing is more important, but still, the beam calibration imperfection bears most of the responsibility.

Finnally, we would like to show the table 4.14 listing all the value of error in $r$ for all instruments rather than the increments $\eta$ to present their actual detectabilities.

TABLE 4.14: Error in $r$ for each experiment, all systematic effects combined.

| Instruments | $\sigma_r^{all}$ |
|---|---|
| LiteBIRD (real) | **0.000428** |
| LiteBIRD | **0.000364** |
| S-4 DW | **0.000346** |
| S-4 UD | **0.000332** |
| SO LAT | **0.001601** |
| SO SAT | **0.000936** |
| PICO | **0.000071** |

PICO has an error in $r$ one magnitude lower than the others. Obviously, its detectability is at the top and followed by CMB-S4, then LiteBIRD, the last is SO.

# Chapter 5

# Summary and prospective

## 5.1 Summary

In this work, we reviewed what the CMB polarization is and its significance in modern cosmological study. We introduced and discussed the obstacles in order to detect the CMB polarization.

We mainly evaluated three relevant kinds of systematic effects generated from calibration processes, polarization angle mismatch, random pointing, and beam calibration imperfection, in terms of the detectability of tensor-to-scalar ratio $r$ for the four relevant future experiments, LiteBIRD, CMB-S4, SO and PICO, which will serve as the main forces in the CMB polarization detection in next decade aiming at $r < 0.001$. These three systematic effects, that are used as interesting examples of many other potential systematic effects to illustrate the their impact on the $r$ uncertainties, are studied individually, and we also took a glimpse onto their combination effect at the end.

The results show that for LiteBIRD, CMB-S4 UD, SO SAT and PICO, the main systematic effects are their beam mis-calibrations; For CMB-S4 DW and SO LAT the beam mis-calibrations affect less.

In order to have the error increment $\eta < 1\%$, PICO and CMB-S4 UD have to have strict polarization angle calibration requirements <5′; while SO LAT does not have to calibrate the polarization angle with a high precision <20′; Others, LiteBIRD, CMB-S4 DW and SO SAT are at the middle, with requirements around 10′.

We believe CMB-S4 and SO LAT already have good calibration in their pointings and generate negligible noises, while LiteBIRD needs to calibrate the pointing around or less than 3.5′, a fraction of $1/8$ of its beam width; SO SAT needs to calibrate the pointing <2.75′, which is a $1/7$ of its beam width; For PICO, it is necessary to calibrate its pointing into the 1′ level, which is hard but obligatory, otherwise its good level of detectability will be very much worsen.

With the typical systematic effects, still, PICO stands at the top among all the four experiments with its excellent detectability on $r$, followed by CMB-S4 and then LiteBIRD. Although the SO has the worst configuration compared to the others, it still has the ability to observe $r < 0.001$ in the future, overwhelming the current experiments.

## 5.2 Prospective

In reality, there are many more kinds of systematic effects than the ones considered in our work, for example, the temperature fluctuation on the focal plane which will influence the detector's gain, the uncertainties in the frequency respond of the detectors within the different bands, the imperfections in the different optical subsystems,

specially the Half Wave Plate that is used to modulate the polarization signal, etc. In the present work we only consider three main systematics as illustrative examples of the kind of effects they can produce, however an exhaustive analysis of all the systematics is necessary in order to have a good control of the instrument and to limit their impact in the $r$ uncertainties and biases.

We also would like to have an analysis with a higher computing power in finer step-size for both polarization angle mismatch and pointing error, e.g., 0.1′ from 0′ to 90′. Besides, the pixel resolution $N_{side}$ should be upgraded from 512 now to at least 2048, which requires 16 times or more computational amount, thus we would suggest to use HPC infrastructures.

We only considered three different frequency bands and three different far-sidelobe types for each experiment because the convolution between maps and beams, and harmonic analysis is really time-consuming currently. We suggested to use more frequency bands and different central beam widths in different frequency bands should be considered as well rather than using a representative one for all frequencies. As for the beam, this is the systematic that is worst modeled except for the case of LiteBIRD, because all the other beam profiles were extrapolated from the measurements from LiteBIRD. Even for LiteBIRD, there are too many degrees of freedom to do the far-sidelobe construction below -50dB, and what we did is just one situation that assumes the largest calibration difference.

$\hat{r}$, the estimator of $r$ was considered only for the case of a null B-mode signal, i.e. $r = 0$. It would be interesting to see how the uncertainties produced by the systematics change for other values of $r \neq 0$. On the other hand, the error of this estimator is determined by the statistical distribution of the sum of Gaussian distributed spherical-harmonic coefficient $a_{\ell m}$, which should follows $\chi^2$ distribution rather than a Gaussian distribution. Therefore, the efficiency of this estimator should be also evaluated, especially for those effects where the low multipoles, $\ell < 30$, are more important.

To have a more comprehensive evaluation on the systematic effects, we should consider the biases in $r$ not only for LiteBIRD's polarization angle mismatch as the work done by [29], but for all and then compare the results with those obtained in the present work that consider the uncertainties in $r$, to see which constrains the systematic effects more.

New methods for a more precise and accurate calibration could be developed, e.g., using a small calibration satellite for those space telescopes[21]. Also, for the case of the polarization angle the 'self-calibration' method, based on the theoretical assumption that EB and TB cross-spectra vanish[54, 56], could be used. However, in this latter case the calibration can be wrong if the theoretical assumption is false.

# Bibliography


[1] Arno A Penzias and Robert Woodrow Wilson. "A measurement of excess antenna temperature at 4080 Mc/s." In: *The Astrophysical Journal* 142 (1965), pp. 419–421.

[2] EK Conklin. "Velocity of the Earth with respect to the Cosmic Background Radiation". In: *Nature* 222.5197 (1969), pp. 971–972.

[3] George F Smoot et al. "Structure in the COBE differential microwave radiometer first-year maps". In: *The Astrophysical Journal* 396 (1992), pp. L1–L5.

[4] John Michael Kovac et al. "Detection of polarization in the cosmic microwave background using DASI". In: *Nature* 420.6917 (2002), pp. 772–787.

[5] Alan H. Guth. "Inflationary universe: A possible solution to the horizon and flatness problems". In: *Phys. Rev. D* 23 (2 Jan. 1981), pp. 347–356. DOI: 10.1103/PhysRevD.23.347. URL: https://link.aps.org/doi/10.1103/PhysRevD.23.347.

[6] Arttu Rajantie. "Magnetic monopoles in field theory and cosmology". In: *Philosophical Transactions of the Royal Society A: Mathematical, Physical and Engineering Sciences* 370.1981 (2012), pp. 5705–5717.

[7] M Tristram et al. "Planck constraints on the tensor-to-scalar ratio". In: *Astronomy & Astrophysics* 647 (2021), A128.

[8] Scott Dodelson. *Modern Cosmology*. Amsterdam: Academic Press, 2003. ISBN: 978-0-12-219141-1.

[9] Herranz Diego and Martínez-González Enrique. *Cosmology 2020-2021*. Spain: A University of Cantabria publication, 2021.

[10] Aritra Das, Ritesh Ghosh, and S Mallik. "Saha ionization equation in the early Universe". In: *The Astrophysical Journal* 881.1 (2019), p. 40.

[11] Meghnad N Saha. "On a physical theory of stellar spectra". In: *Proceedings of the Royal Society of London. Series A, Containing Papers of a Mathematical and Physical Character* 99.697 (1921), pp. 135–153.

[12] Jurgen Ehlers, P Geren, and Rainer K Sachs. "Isotropic Solutions of the Einstein-Liouville Equations". In: *Journal of Mathematical Physics* 9.9 (1968), pp. 1344–1349.

[13] Chris A Clarkson and Richard K Barrett. "Does the isotropy of the CMB imply a homogeneous universe? Some generalized EGS theorems". In: *Classical and Quantum Gravity* 16.12 (Oct. 1999), pp. 3781–3794. ISSN: 1361-6382. DOI: 10.1088/0264-9381/16/12/302. URL: http://dx.doi.org/10.1088/0264-9381/16/12/302.

[14] George Gabriel Stokes. "On the composition and resolution of streams of polarized light from different sources". In: *Transactions of the Cambridge Philosophical Society* 9 (1851), p. 399.

[15] Ruth Durrer. *The Cosmic Microwave Background*. 2nd ed. Cambridge University Press, 2020. DOI: 10.1017/9781316471524.

[16] Marc Kamionkowski and Ely D Kovetz. "The quest for B modes from inflationary gravitational waves". In: *Annual Review of Astronomy and Astrophysics* 54 (2016), pp. 227–269.

[17] Wayne Hu. *Power Spectrum*. http://background.uchicago.edu/~whu/intermediate/map5.html. Accessed: 2021-06-07.

[18] Alexei A Starobinsky. "A new type of isotropic cosmological models without singularity". In: *Physics Letters B* 91.1 (1980), pp. 99–102.

[19] Colin Bischoff. *CMB Polarization*. https://lweb.cfa.harvard.edu/~cbischoff/cmb/. Accessed: 2021-06-09.

[20] Kevork Abazajian et al. *CMB-S4 Science Case, Reference Design, and Project Plan*. 2019. arXiv: 1907.04473 [astro-ph.IM].

[21] Francisco J Casas et al. "L2-CalSat: A Calibration Satellite for Ultra-Sensitive CMB Polarization Space Missions". In: *Sensors* 21.10 (2021), p. 3361.

[22] JA Tauber et al. "Characterization of the in-flight properties of the Planck telescope". In: *Astronomy & Astrophysics* 622 (2019), A55.

[23] R Adam et al. "Planck 2015 results-VII. High Frequency Instrument data processing: Time-ordered information and beams". In: *Astronomy & Astrophysics* 594 (2016), A7.

[24] H. Sugai et al. "Updated Design of the CMB Polarization Experiment Satellite LiteBIRD". In: *Journal of Low Temperature Physics* 199.3-4 (Jan. 2020), pp. 1107–1117. ISSN: 1573-7357. DOI: 10.1007/s10909-019-02329-w. URL: http://dx.doi.org/10.1007/s10909-019-02329-w.

[25] Kevork N. Abazajian et al. *CMB-S4 Science Book, First Edition*. 2016. arXiv: 1610.02743 [astro-ph.CO].

[26] Peter Ade et al. "The Simons Observatory: science goals and forecasts". In: *Journal of Cosmology and Astroparticle Physics* 2019.02 (2019), p. 056.

[27] Shaul Hanany et al. *PICO: Probe of Inflation and Cosmic Origins*. 2019. arXiv: 1902.10541 [astro-ph.IM].

[28] Masashi Hazumi et al. "LiteBIRD satellite: JAXA's new strategic L-class mission for all-sky surveys of cosmic microwave background polarization". In: *Space Telescopes and Instrumentation 2020: Optical, Infrared, and Millimeter Wave* (Dec. 2020). Ed. by Makenzie Lystrup et al. DOI: 10.1117/12.2563050. URL: http://dx.doi.org/10.1117/12.2563050.

[29] Enrique Martínez-González, Patricio Vielva, and FJ Casas-Reinares. "Polar angle requirements for CMB B-mode experiments". In: (2020). URL: https://indico.ipmu.jp/event/380/timetable/?print=1%5C&view=standard.

[30] Charles R. Harris et al. "Array programming with NumPy". In: *Nature* 585.7825 (Sept. 2020), pp. 357–362. DOI: 10.1038/s41586-020-2649-2. URL: https://doi.org/10.1038/s41586-020-2649-2.

[31] J. D. Hunter. "Matplotlib: A 2D graphics environment". In: *Computing in Science & Engineering* 9.3 (2007), pp. 90–95. DOI: 10.1109/MCSE.2007.55.

[32] Andrea Zonca et al. "healpy: equal area pixelization and spherical harmonics transforms for data on the sphere in Python". In: *Journal of Open Source Software* 4.35 (Mar. 2019), p. 1298. DOI: 10.21105/joss.01298. URL: https://doi.org/10.21105/joss.01298.

[33] K. M. Górski et al. "HEALPix: A Framework for High-Resolution Discretization and Fast Analysis of Data Distributed on the Sphere". In: *apj* 622 (Apr. 2005), pp. 759–771. DOI: 10.1086/427976. eprint: arXiv:astro-ph/0409513.

[34] Sara Motalebi. "HEALPix and healpy – with examples". In: (Feb. 2020).

[35] Cullan Howlett et al. "CMB power spectrum parameter degeneracies in the era of precision cosmology". In: *jcap* 1204 (2012), p. 027. DOI: 10.1088/1475-7516/2012/04/027. arXiv: 1201.3654 [astro-ph.CO].

[36] Antony Lewis, Anthony Challinor, and Anthony Lasenby. "Efficient computation of CMB anisotropies in closed FRW models". In: *apj* 538 (2000), pp. 473–476. DOI: 10.1086/309179. arXiv: astro-ph/9911177 [astro-ph].

[37] P. Diego-Palazuelos et al. "Comparison of delensing methodologies and assessment of the delensing capabilities of future experiments". In: *Journal of Cosmology and Astroparticle Physics* 2020.11 (Nov. 2020), pp. 058–058. ISSN: 1475-7516. DOI: 10.1088/1475-7516/2020/11/058. URL: http://dx.doi.org/10.1088/1475-7516/2020/11/058.

[38] Y. Akrami et al. "Planck2018 results". In: *Astronomy & Astrophysics* 641 (Sept. 2020), A10. ISSN: 1432-0746. DOI: 10.1051/0004-6361/201833887. URL: http://dx.doi.org/10.1051/0004-6361/201833887.

[39] European Space Agency. Accessed: 2021. URL: http://pla.esac.esa.int/pla/#cosmology.

[40] B. Thorne et al. "The Python Sky Model: software for simulating the Galactic microwave sky". In: *Monthly Notices of the Royal Astronomical Society* 469.3 (May 2017), pp. 2821–2833. ISSN: 1365-2966. DOI: 10.1093/mnras/stx949. URL: http://dx.doi.org/10.1093/mnras/stx949.

[41] P. A. R. Ade et al. "Planck2015 results". In: *Astronomy & Astrophysics* 594 (Sept. 2016). ISSN: 1432-0746. DOI: 10.1051/0004-6361/201525898. URL: http://dx.doi.org/10.1051/0004-6361/201525898.

[42] C. L. Bennett et al. "NINE-YEAR WILKINSON MICROWAVE ANISOTROPY PROBE ( WMAP ) OBSERVATIONS: FINAL MAPS AND RESULTS". In: *The Astrophysical Journal Supplement Series* 208.2 (Sept. 2013), p. 20. ISSN: 1538-4365. DOI: 10.1088/0067-0049/208/2/20. URL: http://dx.doi.org/10.1088/0067-0049/208/2/20.

[43] M.-A. Miville-Deschênes et al. "Separation of anomalous and synchrotron emissions using WMAP polarization data". In: *Astronomy & Astrophysics* 490.3 (Sept. 2008), pp. 1093–1102. ISSN: 1432-0746. DOI: 10.1051/0004-6361:200809484. URL: http://dx.doi.org/10.1051/0004-6361:200809484.

[44] Jacques Delabrouille et al. "The pre-launch Planck Sky Model: a model of sky emission at submillimetre to centimetre wavelengths". In: *Astronomy & Astrophysics* 553 (2013), A96.

[45] A Kogut. "Synchrotron spectral curvature from 22 MHz to 23 GHz". In: *The Astrophysical Journal* 753.2 (2012), p. 110.

[46] Sigurd K Næss and Thibaut Louis. "Lensing simulations by Taylor expansion—not so inefficient after all". In: *Journal of Cosmology and Astroparticle Physics* 2013.09 (2013), p. 001.

[47] George B. Rybicki and Alan P. Lightman. *Radiative processes in astrophysics*. 1979.

[48] Brian Keating et al. "Large angular scale polarization of the cosmic microwave background radiation and the feasibility of its detection". In: *The Astrophysical Journal* 495.2 (1998), p. 580.

[49] R. Génova-Santos et al. "QUIJOTE scientific results – II. Polarisation measurements of the microwave emission in the Galactic molecular complexes W43 and W47 and supernova remnant W44". In: *Monthly Notices of the Royal Astronomical Society* 464.4 (Oct. 2016), pp. 4107–4132. ISSN: 1365-2966. DOI: 10.1093/mnras/stw2503. URL: http://dx.doi.org/10.1093/mnras/stw2503.

[50] European Space Agency. Accessed: 2021. URL: https://pla.esac.esa.int/#maps.

[51] UChicago. *Sky masks for simulations*. URL: https://cmb-s4.uchicago.edu/wiki/index.php/Sky_masks_for_simulations.

[52] Josquin Errard et al. "Robust forecasts on fundamental physics from the foreground-obscured, gravitationally-lensed CMB polarization". In: *Journal of Cosmology and Astroparticle Physics* 2016.03 (Mar. 2016), pp. 052–052. ISSN: 1475-7516. DOI: 10.1088/1475-7516/2016/03/052. URL: http://dx.doi.org/10.1088/1475-7516/2016/03/052.

[53] P Diego-Palazuelos et al. "Comparison of delensing methodologies and assessment of the delensing capabilities of future experiments". In: *Journal of Cosmology and Astroparticle Physics* 2020.11 (2020), p. 058.

[54] Yuto Minami et al. "Simultaneous determination of the cosmic birefringence and miscalibrated polarization angles from CMB experiments". In: *Progress of Theoretical and Experimental Physics* 2019.8 (2019), 083E02.

[55] Hayato Takakura et al. "Far-Sidelobe Antenna Pattern Measurement of LiteBIRD Low Frequency Telescope in 1/4 Scale". In: *IEEE Transactions on Terahertz Science and Technology* 9.6 (2019), pp. 598–605. DOI: 10.1109/TTHZ.2019.2937497.

[56] Yuto Minami. "Determination of miscalibrated polarization angles from observed cosmic microwave background and foreground EB power spectra: Application to partial-sky observation". In: *Progress of Theoretical and Experimental Physics* 2020.6 (2020), 063E01.

[57] Daniel Baumann. "TASI Lectures on Primordial Cosmology". In: *arXiv preprint arXiv:1807.03098* (2018).

[58] Andrew R Liddle, Paul Parsons, and John D Barrow. "Formalizing the slow-roll approximation in inflation". In: *Physical Review D* 50.12 (1994), p. 7222.

[59] A. G. Polnarev. "Polarization and Anisotropy Induced in the Microwave Background by Cosmological Gravitational Waves". In: *sovast* 29 (Dec. 1985), pp. 607–613.

[60] Robert Crittenden, Richard L. Davis, and Paul J. Steinhardt. "Polarization of the Microwave Background Due to Primordial Gravitational Waves". In: *The Astrophysical Journal* 417 (Nov. 1993), p. L13. ISSN: 1538-4357. DOI: 10.1086/187082. URL: http://dx.doi.org/10.1086/187082.

[61] Arthur Kosowsky. "Cosmic microwave background polarization". In: *Annals Phys.* 246 (1996), pp. 49–85. DOI: 10.1006/aphy.1996.0020. arXiv: astro-ph/9501045.

[62] Matias Zaldarriaga and Uroš Seljak. "All-sky analysis of polarization in the microwave background". In: *Physical Review D* 55.4 (1997), p. 1830.

[63] Uros Seljak and Matias Zaldarriaga. "A line of sight approach to cosmic microwave background anisotropies". In: *arXiv preprint astro-ph/9603033* (1996).

[64] Berkeley. *Scalar Perturbations*. https://w.astro.berkeley.edu/~mwhite/polar/node4.html. Accessed: 2021-06-09.

# Appendix A

# Stokes parameters

## A.1 Another expression of the Stokes parameter

When we consider the propagation direction is $z$ and polarization direction is $x$ and $y$[9],

$$\begin{aligned} E_x &= a_x(t)\cos\left[\omega_0 t - \theta_x(t)\right] \\ E_y &= a_y(t)\cos\left[\omega_0 t - \theta_y(t)\right] \end{aligned} \tag{A.1}$$

and the Stokes parameters are

$$\begin{aligned} I &\equiv \left\langle a_x^2 \right\rangle + \left\langle a_y^2 \right\rangle \\ Q &\equiv \left\langle a_x^2 \right\rangle - \left\langle a_y^2 \right\rangle \\ U &\equiv \left\langle 2a_x a_y \cos\left(\theta_x - \theta_y\right) \right\rangle \\ V &\equiv \left\langle 2a_x a_y \sin\left(\theta_x - \theta_y\right) \right\rangle . \end{aligned} \tag{A.2}$$

## A.2 Spin-2 properties of polarization tensor

When rotate the direction basis with an angle $\alpha$ around the $\boldsymbol{n}$ axis, the basis changes[15]

$$\left(\boldsymbol{\epsilon}^{(1)}, \boldsymbol{\epsilon}^{(2)}\right) \Rightarrow \left(\boldsymbol{\epsilon}^{(1)}\cos\alpha + \boldsymbol{\epsilon}^{(2)}\sin\alpha, -\boldsymbol{\epsilon}^{(1)}\sin\alpha + \boldsymbol{\epsilon}^{(2)}\cos\alpha\right), \tag{A.3}$$

consequently, the coefficients of the electric field with respect to the rotated basis are

$$\begin{aligned} E_1' &= E_1\cos(2\alpha) + E_2\sin(2\alpha) \\ E_2' &= -E_1\sin(2\alpha) + E_2\cos(2\alpha). \end{aligned} \tag{A.4}$$

which naturally gives the change of the Stokes parameters

$$\begin{aligned} I' &= I \\ V' &= V \\ Q' &= Q\cos(2\alpha) + U\sin(2\alpha) \\ U' &= -Q\sin(2\alpha) + U\cos(2\alpha). \end{aligned} \tag{A.5}$$

Or,

$$\begin{bmatrix} Q & U \\ U & -Q \end{bmatrix} \Rightarrow \begin{bmatrix} \cos\alpha & \sin\alpha \\ -\sin\alpha & \cos\alpha \end{bmatrix} \begin{bmatrix} Q & U \\ U & -Q \end{bmatrix} \begin{bmatrix} \cos\alpha & -\sin\alpha \\ \sin\alpha & \cos\alpha \end{bmatrix}. \tag{A.6}$$

Here we can have another clearer physical explanation on the Stokes parameter $U$: If we set the angle $\alpha = 45$ degree, then $U$ turns into $Q$ and $Q$ turns into $-U$. Thus we can say $U$ is a quantity measures the difference of the linear polarization between

two new polarization basis which is rotated $-45$ degree from the original basis $\boldsymbol{\epsilon}^{(1)}$ and $\boldsymbol{\epsilon}^{(2)}$.

## A.3 E-mode and B-mode as electric-field-like and magnetic-field-like polarizations

These two operators $\eth$ and $\eth^*$ behave like derivative, see Appendix 4.2.4 in [15]:

$$\begin{aligned}\eth &= -\sqrt{2}\nabla_{\boldsymbol{e}_-}\\ \eth^* &= -\sqrt{2}\nabla_{\boldsymbol{e}_+}.\end{aligned} \tag{A.7}$$

Then when we look back to (1.13) and (1.7), we can rewrite them into

$$\begin{aligned}(\eth^*)^2(Q+iU)(\boldsymbol{n}) &= 2\nabla_{\boldsymbol{e}_-}\nabla_{\boldsymbol{e}_-}\mathcal{P}_{++}\\ \eth^2(Q-iU)(\boldsymbol{n}) &= 2\nabla_{\boldsymbol{e}_+}\nabla_{\boldsymbol{e}_+}\mathcal{P}_{--},\end{aligned} \tag{A.8}$$

the E mode and B mode can turn into

$$\begin{aligned}\mathcal{E} &= \nabla_{\boldsymbol{e}_-}\nabla_{\boldsymbol{e}_-}\mathcal{P}_{++} + \nabla_{\boldsymbol{e}_+}\nabla_{\boldsymbol{e}_+}\mathcal{P}_{--} = 2\nabla_i\nabla_j\mathcal{P}_{ij}\\ \mathcal{B} &= \nabla_{\boldsymbol{e}_-}\nabla_{\boldsymbol{e}_-}\mathcal{P}_{++} + \nabla_{\boldsymbol{e}_+}\nabla_{\boldsymbol{e}_+}\mathcal{P}_{--} = 2\epsilon_{lm}\epsilon_{ij}\nabla_l\nabla_i\mathcal{P}_{jm}.\end{aligned} \tag{A.9}$$

Now we see the meaning of $\mathcal{E}$ and $\mathcal{B}$. The former is a gradient type and the latter is a curl type, just like electric field and magnetic field, but without having any physial relation with electric field or magnetic field.

However $\mathcal{E}$ and $\mathcal{B}$ are global quantities and do not have direct interpretation on the measurable polarization $Q \pm iU$[15]. In the next chapter we will see how it give us information about the primordial perturbations.

Until now we are discussing the generalized picture that the analysis is done on the curved celestial shpere. For the analysis on the flat sky, as an approximation of a small region on the sphere, the situation is much easier, so here we omit it.

## A.4 Physical meaning of the Stokes parameters

Let´s come to the physical meaning of the Stokes parameters. Without comment, $I$ is the intensity of the electromagnetic wave. $Q$ is the difference between the intensities of the light polarized in $\boldsymbol{\epsilon}^{(1)}$ and the one polarized in $\boldsymbol{\epsilon}^{(2)}$. In other words, if $Q$ is positive, the $\boldsymbol{\epsilon}^{(1)}$ light is stronger than $\boldsymbol{\epsilon}^{(2)}$ light and vice versa. But $Q$ does not provide the information about the phase difference between these two light, for example, $Q = 0$ light has three possibilities: maximally linearly polarized in the direction in the middle of two polarization directions; maximally circularly polarized; mixed with linearly polarized light and circularly polarized light.

$U$ and $V$ measures the correlation between these two lights, involving their phase difference. For example in (A.1), if the phase difference between $E_x$ and $E_y$ is 0 or $\pi$, then the light is maximally linearly polarized in the direction between $x$ and $y$. Here $Q = \pm Q_{max} = \pm\langle 2a_x a_y\rangle$ and $V = 0$; if the phase difference is $\pi/2$, the light is maximally circularly polarized, $V = \pm V_{max} = \pm\langle 2a_x a_y\rangle$, $Q = 0$. So we can see that $Q$ represents the level of linear polarization, while $V$ represents the intensity difference between left-handed circular polarization and right-handed circular polarization. $|Q|$ wanes and $|V|$ waxes and vice versa.

# Appendix B

# Inflation Kinematics and Perturbations

We agree that we are under FLRW metric

$$ds^2 = -c^2dt^2 + a^2(t)\left[d\boldsymbol{x}^2 + k\frac{(\boldsymbol{x}\cdot d\boldsymbol{x})^2}{1-k\boldsymbol{x}^2}\right], \tag{B.1}$$

where our universe is isotropic, homogeneous and under goes expanding[9].

The Friedmann equations, denote the Einstein equations (describes the spacetime dynamic) in the FLRW spacetime are

$$\begin{aligned} H^2 &= \frac{8\pi G}{3}a^2\rho - K \\ \dot{H} &= -\frac{4\pi G}{3}a^2(\rho+3). \end{aligned} \tag{B.2}$$

## B.1 Inflation theory and its simplest kinematics

Inflation theory has not be proved and it sounds like a crazy and bizarre idea but can effectively and elegantly solve three big cosmological problems: Horizon problem, Flatness problem an magnetic monopole problem at once. The properties and parameters of the inflation can be fixed through solving the horizon problem, that we think it´s impossible for nearly 40000 patches in the sky to have the same properties. Because are mutually disconnected because their Hubble radius(denotes the farthest distance that information can travel) is not large enough to cover the other.

How to solve horizon problem? One assumption is they were connected in a very small region, so they talked with each other and got the same physical properties. Then they were stretched away from each other, makes us to think that they were not causally connected. This 'spacetime stretching' requires a simple condition at the early universe[57]

$$\frac{d}{dt}(aH)^{-1} = -\frac{\left(\frac{\dot{H}}{H^2}+1\right)}{a} = \frac{d}{dt}(\dot{a})^{-1} = -\frac{\ddot{a}}{(\dot{a})^2} < 0, \tag{B.3}$$

means the Hubble distance $\frac{c}{H}$ increases more slowly than the scale factor, things which were causally connected before the inflation exited the horizon super fast. As explained in[8], regions that we observed to be astronomical today were actually microscopically small before the inflation and were in causal contact with each other, then were pushed away from each other by the inflation and can no longer have

communication. On the other hand, this implies an accelerated expansion

$$\ddot{a} > 0, \tag{B.4}$$

and

$$-\frac{\dot{H}}{H^2} < 1. \tag{B.5}$$

By observation we found actually $-\frac{\dot{H}}{H^2} \ll 1$. It implies $\dot{H} \sim 0$. But $\dot{H} \neq 0$ is needed to end the inflation. So approximately $H \sim$ const.

The relation between the scale factor and Hubble parameter thus performs like a differential equation: $\dot{a} = Ha$, it gives the solution of the scale factor

$$a(t) \propto e^{Ht}, \tag{B.6}$$

Which is similar to today´s accelerating expanding universe, dominated by the cosmological constant term, i.e. dark energy.

By the way, during the inflation, the metric is

$$ds^2 = -c^2dt^2 + a_{ini}^2 e^{2Ht}\left[d\boldsymbol{x}^2 + k\frac{(\boldsymbol{x}\cdot d\boldsymbol{x})^2}{1-k\boldsymbol{x}^2}\right], \tag{B.7}$$

Inflation will not happen automatically because it violates the strong energy condition if there is only a radiation and matter domination without any inflation field. Normally, Hubble distance $\frac{c}{H}$ is increasing faster than the expansion with a expression in contrast with (B.3): $\frac{d}{dt}(aH)^{-1} > 0$.

In the simplest model, the inflation was driven by one scalar field $\phi$ called inflaton. The choice on the scalar fields (sometimes there are more than one field) is due to historical reason when particle physicists were studying the extension of the Standard Model. It´s true that there are also some vector field inflation theories work as well[8].

QFT tell us a single scalar field´s Lagrangian $\mathcal{L} = \frac{1}{2}\phi\Box\phi - V(\phi)$ and energy-momentum tensor. We consider the inflaton was dominated at that time, matter, radiation etc. are not taken into account. Inflaton's equation of motion (EoM) in an FLRW spacetime can be derived from combining Friedmann equation and the energy density obtained from its energy-momentum tensor[16], which is Klein-Gordon equation[9]

$$\ddot{\phi} + 3H\dot{\phi} + \frac{dV(\phi)}{d\phi} = 0. \tag{B.8}$$

The expansion is coupled with the inflaton in the second term $3H\dot{\phi}$.

Whether the inflation will happen and how long it will last are depending on the potential $V(\phi)$ which can be very different from one to another, and the term $3H\dot{\phi}$ which acts on the field like a reducer or friction. One simplest model is single-field slow-roll inflation where 'slow-roll' is normally advertised as requiring the smallness of two parameters which are respectively proportional to $\left(\frac{V'}{V}\right)^2$ and $\frac{V''}{V}$[58], meaning that the potential is relatively flat. There is another 'slow-roll' refers to the small changing of the Hubble parameter $H(\phi)$[58].

## B.2 Perturbation theory

After we proposed the inflation and studied its behavior, the perturbation before the inflation comes into our mind. The inflation played a role like a magnifier: it stretched the primordial fluctuation into a relatively mutually-unconnected large scale in a short time before they had adequate time or sufficiently small distance to be appeased. The fluctuation at that time made a imprint in the CMB at LSS and then became the seeds of the structure formation.

The perturbation of the spacetime can be categorized into 2 kinds: scalar perturbation and tensor perturbation.

### B.2.1 Scalar perturbation

First we are going to think the inflaton $\phi$´s variation in space. Because inflaton $\phi$ was dominating at the beginning, its fluctuation can induce energy density fluctuation and then cause the spacetime fluctuation. with a curvature perturbation $\mathcal{R}(x,t)$. Under the comoving gauge $g_{0\mu} = 0$, the space components of the metric is[16]

$$g_{ij} = a(t)^2 e^{2\mathcal{R}(x,t)}\delta_{ij}, \tag{B.9}$$

and in terms of Bardeen variables the curbature perturbation is given by

$$R = -\frac{2}{3(1+\omega)}\left[\Psi + \frac{\dot{\Phi}}{H}\right] + \Phi. \tag{B.10}$$

With a new field variable $v^2 = 2M_{Pl}^2\epsilon\mathcal{R}$, the action is

$$\begin{aligned} S_{\mathcal{R}} &= \int \mathrm{d}t \int \mathrm{d}^3\boldsymbol{x}a^3\left[\frac{1}{2}\dot{v}^2 - \frac{1}{2}(\nabla v)^2/a^2\right] \\ &= \sum_k \int \mathrm{d}t a^3\left[\frac{1}{2}\left|\dot{v}_k\right|^2 - \frac{k^2}{2a^2}\left|v_k\right|^2\right], \end{aligned} \tag{B.11}$$

expressed in an ensemble of oscillators, from the canonical quantization treatment to the field.

We would have equation of motion from variations of the action in terms of those Fourier modes,

$$\ddot{v}_k + 3H\dot{v}_k + \left(\frac{k}{a}\right)^2 v_k = 0. \tag{B.12}$$

Its solution can be written in following form

$$v_k(t) = \frac{H}{(2k^3)^{1/2}}\left(i + \frac{k}{aH}\right)e^{-ik/aH}, \tag{B.13}$$

The field went out at late times when $k \ll aH$, and $\left|v_k\right|^2 \to \frac{H^2}{2k^3}$, meaning that inflation converts subhorizon quantum fluctuations in the curvature to classical superhorizon curvature perturbations[16], as we mentioned before.

Providing the amplitude $\mathcal{R}_k$ a Gaussian variance

$$\left\langle\left|\mathcal{R}_k\right|^2\right\rangle = \frac{H^2}{M_{\mathrm{Pl}}^2\epsilon k^3}, \tag{B.14}$$

after adding all the Fourier modes together, $\left\langle \mathcal{R}^2 \right\rangle = \int \mathrm{d}\ln k \Delta^2_{\mathcal{R}}(k)$, this gives the curvature variance in real space. We can then define the power spectrum of the curvature perturbation after applying slow-roll approximation

$$\Delta^2_{\mathcal{R}}(k) \equiv \frac{k^3}{2\pi^2}\left\langle |\mathcal{R}|^2 \right\rangle = \frac{1}{8\pi^2}\frac{H^2}{M^2_{\rm Pl}\epsilon} \simeq \frac{1}{24\pi^2}\frac{V}{M^4_{\rm Pl}\epsilon} = \frac{1}{12\pi^2}\frac{V^3}{M^6_{\rm Pl}(V')^2}. \tag{B.15}$$

The spectral index $n_s$ is defined in a $k$-dependent power law description of $\Delta_{\mathcal{R}}$,

$$\Delta^2_{\mathcal{R}}(k) \equiv A_s \left(\frac{k}{k_*}\right)^{n_s-1}, \tag{B.16}$$

with a reference $k_*$. Then

$$n_s - 1 \equiv \frac{\mathrm{d}\log\Delta^2_{\mathcal{R}}(k)}{\mathrm{d}\log k} \simeq -2\epsilon + \zeta = -3M^2_{Pl}\left(\frac{V'}{V}\right)^2 + 2M^2_{Pl}\frac{V''}{V}. \tag{B.17}$$

The reason that there is a $-1$ in the expression is a historical problem about the convention. There is no problem that we just ignore it, and we will see for tensor perturbation the spectral index is without $-1$.

Spectral index is a very important parameter in the cosmology. We easily can see that under the slow-roll approximation the curvature spectral index is depending on the potential term of the inflaton and its first, second derivatives. Different inflatons, i.e., one scalar field, multiple scalar fields, vector field, can give different indices. Therefore observing and determining the spectral index can help cosmologists rule out many inflation models.

### B.2.2 Tensor perturbation

Then let's start the investigation about the primordial gravitational wave (PGW), sometimes also called inflationary gravitational wave (IGW). Adding a TT gauge gravitational wave (Transverse-traceless gauge), the perturbed metric becomes

$$g_{ij} = a^2\left(\delta_{ij} + 2h_{ij}\right), \tag{B.18}$$

and we can insert it into Einstein-Hilbert action

$$S = \frac{M^2_{pl}}{2}\int d^4x\sqrt{-g}R. \tag{B.19}$$

Once we expand the action we can re-express it in terms of Fourier modes and two polarizations of the gravitational wave $h_+$ and $h_\times$ [1], similarly with a new variable $v_p = \frac{M_{Pl}}{2}h_p$ where $p$ denotes the two polarizations $+$ and $\times$:

$$\begin{aligned} S &= \frac{1}{4}\int \mathrm{d}t \int \mathrm{d}^3\boldsymbol{x} a^3 M^2_{\rm Pl}\left[\frac{1}{2}\left(\dot{h}_{ij}\right)^2 - \frac{1}{2a^2}\left(\partial_k h_{ij}\right)^2\right] \\ &= \sum_{p=+,\times}\sum_k \int \mathrm{d}t a^3\left[\frac{1}{2}\left|\dot{v}_{p,k}\right|^2 - \frac{k^2}{2a^2}\left|v_{p,k}\right|^2\right]. \end{aligned} \tag{B.20}$$

[1] TT gauge gives $\left(h^{\rm TT}_{\mu\nu}\right) = \begin{pmatrix} 0 & 0 & 0 & 0 \\ * & h_+ & h_\times & 0 \\ * & * & -h_+ & 0 \\ * & * & * & 0 \end{pmatrix}$, and $h_{+,\times} = h_{+,\times}(t \pm z/c)$, or in conformal time $h_+(x,\eta) \simeq h(\eta)e^{ik\eta}e^{-ikz}$.

As an analogy to the action of scalar perturbation (B.11), we can have a very similar equation of motion for the Fourier modes of the perturbation variable with 2 polarization kinds and then an exactly similar tensor power spectrum

$$\Delta_t^2(k) \equiv 2\frac{k^3}{2\pi^2}\left\langle \left|h_{p,k}\right|^2 \right\rangle = \frac{2}{\pi^2}\frac{H^2}{M_{\rm Pl}^2}. \tag{B.21}$$

Also similarly, in power law

$$\Delta_t^2(k) \equiv A_t \left(\frac{k}{k_*}\right)^{n_t}, \tag{B.22}$$

The spectral index is

$$n_t = \frac{\mathrm{d}\ln\Delta_h^2(k)}{\mathrm{d}\ln k} = -2\epsilon \simeq -M_{Pl}^2\left(\frac{V'}{V}\right)^2, \tag{B.23}$$

depending on the inflaton potential and its first derivative, and it is negative indicating a red sprectrum of the PGW.

## B.3 Perturbation to CMB

How these two perturbation, density wave and PGW, effect relatively to the CMB polarization? Well, we need to see how photons were affected by the perturbation.

In terms of a single monochromatic, plane-wave-like, polarized gravitational wave traveling in the direction of $z$, the metric in(B.18) can be written as

$$\mathrm{d}s^2 = a^2(\eta)\left[\mathrm{d}\eta^2 - \mathrm{d}x^2\left(1+h_+\right) + \mathrm{d}y^2\left(1-h_+\right) + \mathrm{d}z^2\right], \tag{B.24}$$

and $h(\boldsymbol{x},\eta) \simeq h(\eta)e^{ik\eta}e^{-ikz}$[59].

Propagating photons with a cosine of the traveling angle between $z$ axis $\mu$ and a azimuthal angle $\phi$ experience a frequency change due to the expansion of the spacetime:

$$\frac{1}{\nu}\frac{\mathrm{d}\nu}{\mathrm{d}\eta} = -\frac{1}{2}\left(1-\mu^2\right)\cos 2\phi e^{-ikz}\frac{\mathrm{d}}{\mathrm{d}\eta}\left(he^{ik\eta}\right). \tag{B.25}$$

So far there is no polarization, but a radiation field with anisotropic energy distribution. However, as we have seen in the Thomson scattering section that this radiation field with anisotropic energy distribution will induce polarization.

To quantify the polarization, distribution functions $\bar{f}_s(\boldsymbol{q},\boldsymbol{x};\eta)$ for four Stokes parameters $s = I, Q, U, V$ are necessary, here the photons have momentum $\boldsymbol{q}$. First, the unperturbed distribution functions are

$$\begin{aligned}
\bar{f}_I(\boldsymbol{q},\boldsymbol{x};\eta) &= \frac{1}{e^{h\upsilon/k_{\rm B}T(\eta)}-1}\\
\bar{f}_Q(\boldsymbol{q},\boldsymbol{x};\eta) &= 0\\
\bar{f}_U(\boldsymbol{q},\boldsymbol{x};\eta) &= 0\\
\bar{f}_V(\boldsymbol{q},\boldsymbol{x};\eta) &= 0,
\end{aligned} \tag{B.26}$$

where $T(\eta)$ is the unperturbed temperature at comformal time $\eta$, which again remind us an unpolarized perfect black-body radiation of CMB.

Then define perturbations

$$\Delta_s e^{i\boldsymbol{k}\cdot\boldsymbol{x}} = 4\delta f_s/(\partial\bar{f}/\partial \ln T). \tag{B.27}$$

We know no circular polarization is produced in Thomson scattering so $\Delta_V = 0$, and we can extract a perturbation variables $\tilde{\Delta}_s(\mu,\eta)$ only depending on $\mu$ from each $\Delta_s$:

$$\begin{aligned}\Delta_I &= \tilde{\Delta}_I(1-\mu)^2\cos 2\phi\\ \Delta_Q &= \tilde{\Delta}_Q(1+\mu)^2\cos 2\phi\\ \Delta_U &= \tilde{\Delta}_U 2\mu\sin 2\phi = -\tilde{\Delta}_Q 2\mu\sin 2\phi.\end{aligned} \tag{B.28}$$

Then we just directly show the results of the Boltzmann equations [2] for the distribution functions[60][61]:

$$\begin{aligned}\dot{\tilde{\Delta}}_I + ik\mu\tilde{\Delta}_T &= -\dot{h} - \dot{\kappa}[\tilde{\Delta}T - \Psi]\\ \dot{\tilde{\Delta}}_Q + ik\mu\tilde{\Delta}_Q &= -\dot{\kappa}\left[\Delta_P + \Psi\right].\end{aligned} \tag{B.30}$$

The left hand side means the Lagrangian time derivatives for a Fourier mode of wave number $k$.

Some new variables above are

$$\begin{aligned}\Psi &\equiv \left[\frac{1}{10}\tilde{\Delta}_{I0} + \frac{1}{7}\tilde{\Delta}_{T2} + \frac{3}{70}\tilde{\Delta}_{T4} - \frac{3}{5}\tilde{\Delta}_{Q0} + \frac{6}{7}\tilde{\Delta}_{Q2} - \frac{3}{70}\tilde{\Delta}_{Q4}\right]\\ \tilde{\Delta}_{s\ell}(\eta) &= (1/2)\int_{-1}^{1} \mathrm{d}\mu\tilde{\Delta}_s(\mu;\eta)P_\ell(\mu),\end{aligned}$$

and a Thomson optical depth contribution in a interval $d\eta$: $\dot{\kappa}\delta = \frac{d\kappa}{d\eta}d\eta$ which takes part when scattering happened.

The equations (B.30) are then solved numerically.

## B.4 Perturbations to E-mode and B-mode

### B.4.1 E,B-modes from PGW

We show the results of the polarization tensor by PGW[61]

$$\mathcal{P}^{ab}_{k,+}(\theta,\phi) = \frac{T_0}{4\sqrt{2}}\sum_\ell (2\ell+1)P_\ell(\cos\theta)\tilde{\Delta}_{Q\ell}\begin{bmatrix}\left(1+\cos^2\theta\right)\cos 2\phi & 2\cot\theta\sin 2\phi\\ 2\cot\theta\sin 2\phi & -\left(1+\cos^2\theta\right)\csc^2\theta\cos 2\phi\end{bmatrix}. \tag{B.31}$$

The terms $\cos 2\phi$ suggest a quadrupole.

[2] Boltzmann equation describes the statistical behaviour of a thermodynamic system not in a state of equilibrium, devised by Ludwig Boltzmann in 1872. It´s unintegrated form is schematically

$$\frac{df}{dt} = C[f], \tag{B.29}$$

where $C[f]$ is all the collision terms[8].

From (B.31) to harmonics coefficients[62]

$$
\begin{aligned}
a_{\ell m}^{\mathrm{E}\,k,+} &= \frac{\sqrt{\pi(2\ell+1)}}{4\left(\delta_{m,2}+\delta_{m,-2}\right)^{-1}}\left[\frac{(\ell+2)(\ell+1)\tilde{\Delta}_{Q,\ell-2}}{(2\ell-1)(2\ell+1)}+\frac{6\ell(\ell+1)\tilde{\Delta}_{Q\ell}}{(2\ell+3)(2\ell-1)}+\frac{\ell(\ell-1)\tilde{\Delta}_{Q,\ell+2}}{(2\ell+3)(2\ell+1)}\right] \\
a_{\ell m}^{\mathrm{B}\,k,+} &= \frac{-i}{2\sqrt{2}}\sqrt{\frac{2\pi}{(2\ell+1)}}\left(\delta_{m,2}-\delta_{m,-2}\right)\left[(\ell+2)\tilde{\Delta}_{Q,\ell-1}+(\ell-1)\tilde{\Delta}_{Q,\ell+1}\right].
\end{aligned}
\tag{B.32}
$$

The B-mode in $z$ direction and $+$ polarization is

$$
C_\ell^{\mathrm{BB},k,+}=\frac{1}{2l+1}\sum_m\left|a_{\ell m}^B\right|^2=\frac{\pi}{2}\left(\frac{\ell+2}{2\ell+1}\tilde{\Delta}_{Q,\ell-1}+\frac{\ell-1}{2\ell+1}\tilde{\Delta}_{Q,\ell+1}\right)^2. \tag{B.33}
$$

Sum over the Fourier modes and the polarization states we have the total B-mode spectrum

$$
C_\ell^{\mathrm{BB}}=\frac{1}{2\pi}\int k^2\,\mathrm{d}k\left[\frac{\ell+2}{2\ell+1}\tilde{\Delta}_{Q,\ell-1}(k)+\frac{\ell-1}{2\ell+1}\tilde{\Delta}_{Q,\ell-1}(k)\right]^2. \tag{B.34}
$$

Same for E-mode and then numerical solutions are given by[63]

$$
\begin{aligned}
C_\ell^{\mathrm{EE}} &= \int \mathrm{d}\ln k\Delta_h^2(k)\left\{\int_0^{\eta_0-\eta_{\mathrm{ls}}}\mathrm{d}x g\left(\eta_0-x\right)\Psi\left(\eta_0-x\right)\left[-j_\ell(x)+j_\ell''(x)+\frac{2j_\ell(x)}{x^2}+\frac{4j_\ell'(x)}{x}\right]\right\}^2 \\
C_\ell^{\mathrm{BB}} &= \int \mathrm{d}\ln k\Delta_h^2(k)\left\{\int_0^{\eta_0-\eta_{ls}}\mathrm{d}x g\left(\eta_0-x\right)\Psi\left(\eta_0-x\right)\left[2j_\ell'(x)+\frac{4j_\ell(x)}{x}\right]\right\}^2.
\end{aligned}
\tag{B.35}
$$

We can draw a simple conclusion that both polarization mode, B-mode and E-mode are generated by PGW.

### B.4.2 E,B-modes from density perturbation

In density fluctuation, let us consider the quadrupole component of the temperature pattern seen by an observer located in a trough of a plane density wave (think about a stick with cold head and bottom but hot middle or inversely, hot head and bottom but cold middle). The azimuthal symmetry in the problem requires that $\boldsymbol{k}||\boldsymbol{v}$ where $\boldsymbol{v}$ is the flow of the photon, and hence the flow is irrotational $\nabla\times\boldsymbol{v}$ . Because hotter photons from the crests flow into the trough from the $\pm\boldsymbol{k}$ directions while cold photons surround the observer in the plane, the quadrupole pattern seen in a trough has an quadrupolar harmonic with $m=0$[64]:

$$
Y_2^0=3\cos^2\theta-1, \tag{B.36}
$$

where $\theta$ is the angle between direction $\boldsymbol{n}$ and $\boldsymbol{k}$.

The sense of the quadrupole moment determines the polarization pattern through Thomson scattering (remember the incoming anisotropy causes net polarization). Any electron at the LSS now sees a quadrupolar intensity variation that is aligned with the $\theta$ direction or the direction perpendicular[16]. Then This pattern represents a pure $Q$-field on the sky whose amplitude varies in angle as an $\ell=2, m=0$ tensor or a spin-2 field with[64]:

$$
\begin{aligned}
Q(\boldsymbol{n}) &= \sin^2\theta \\
U(\boldsymbol{n}) &= 0.
\end{aligned}
\tag{B.37}
$$

Then the polarization tensor could be written as

$$\mathcal{P}^{ab}(\theta,\phi) = \sum_{\ell} \sin^2\theta \tilde{\Delta}^s_{Q\ell} P_\ell(\cos\theta) \begin{bmatrix} 1 & 0 \\ 0 & -\csc^2\theta \end{bmatrix}. \tag{B.38}$$

An important quantitative conclusion can be drawn that no B-mode was produced in the density perturbation because $\mathcal{P}^{ab}$ is diagonal, and from the definition (A.9), we know that $\mathcal{P}^{ab}\epsilon^c_b = 0$.

In other words, B-mode polarization is a unique imprint of the PGW, and PGW is the direct product of inflation. Therefore scientists are desiring to observe B-mode and then fix the tensor-to-scalar ratio $r$, which are so crucial to certify or falsify the inflation theory and determine the inflaton parameters.